Printed supercapacitors
Project report

Authors: Jari Keskinen, Elina Jansson, Leo von Hertzen, Elina Yli-Rantala, Tiina Maaninen, Salme Jussila, Max Johansson, Tommi Remonen, Fredrik Pettersson, Sami Kielosto, Kim Eiroma, Timo Flyktman, Vidar Grönberg, Yanxi Zhang, Anja Ranta, Carl-Eric Wilén, Ronald Österbacka, Pertti Kauranen, Tony Munter, Kirsi Tappura

Confidentiality: Public

Report's title		
Printed supercapacitors, Project report		
Customer, contact person, address		**Order reference**
Tekes and six industrial companies		Tekes 40044/12
Project name		**Project number/Short name**
Printed supercapacitors		77085, PRISU
Authors		**Pages**
Jari Keskinen, Elina Jansson, Leo von Hertzen, Elina Yli-Rantala, Tiina Maaninen, Salme Jussila, Max Johansson, Tommi Remonen, Fredrik Pettersson, Sami Kielosto, Kim Eiroma, Timo Flyktman, Vidar Grönberg, Yanxi Zhang, Anja Ranta, Carl-Eric Wilén, Ronald Österbacka, Pertti Kauranen, Tony Munter, Kirsi Tappura		66
Keywords		**Report identification code**
supercapacitor, printed power source, printing, energy storage		VTT-R-02902-14

Summary

The report covers the work done in the Printed supercapacitors project during April 2012-March 2014. The aim of the project was to develop manufacturing methods and materials for inexpensive supercapacitors to be used e.g. in smart packaging, active-RFID and other applications requiring energy storage devices.

Supercapacitors were printed on various substrates such as aluminium-polymer laminates and aluminium foils. The electrodes were made mainly of activated carbon that was applied as ink. Also oxide electrodes were developed. The electrolyte choice was wide including aqueous and organic alternatives as well as room-temperature ionic liquids. The materials were first tested in laboratory scale and then applied also in pilot scale printing process.

To demonstrate the developed supercapacitors two different applications were constructed: an active RFID tag powered by a hybrid supercapacitor - solar cell system and a device to supply energy for an electric motor system lifting a weight.

Confidentiality	Public

Tampere 10.6.2014

Written by	Reviewed by	Accepted by
Jari Keskinen Senior Scientist	Kirsi Tappura Principal Scientist	Tuulamari Helaja Head of Research Area

VTT's contact address

Jari Keskinen, PO Box 1300, 33101 Tampere, jari.keskinen@vtt.fi

Distribution (customer and VTT)

Confidex Oy, Kabus Oy, Kemet Electronics Oy, Kone Oyj, Stora Enso Oyj, Walki Oy, Åbo Akademi PCC, Åbo Akademi FunMat, Aalto University Automation Technology, VTT

Preface

This text describes the work done in Printed supercapacitor (PRISU) project. Its purpose is to summarize the work done.

The project was financed by Tekes, six industrial companies and three research partners. The research partners of the project were VTT, Aalto University and Åbo Akademi.

Tampere, Espoo, Oulu, Turku 10.6.2014

The authors

Abstract

The aim of the project was to facilitate supercapacitor manufacturing process by printing technology. This enables low-cost manufacturing process that is important in order to widen the application range of supercapacitors.

Since the focus of the project was in the development of inexpensive alternatives, activated carbon and manganese oxide electrodes were used. Commercial activated carbon was the main electrode material of choice. MnO_2 and bio based activated carbon materials were synthesized. MnO_2 showed higher specific capacitance than commercial activated carbon.

Preparing carbon from kraft lignin using hydrothermal carbonization (HTC) process was developed. Impurities were removed by washing the HTC carbon extensively, but not enough improvement was achieved to enable the use of HTC carbon from lignin directly in printed capacitors. When sucrose was used as precursor the HTC process combined with chemical activation resulted to relatively pure activated carbon for which over 60 F/g specific capacitance (single electrode value) was obtained.

The activated carbon powder used in the electrodes was bound with chitosan in the case of aqueous and ionic liquid electrodes. With organic electrolyte carboxymethyl cellulose (CMC) was found to work even better than polyvinylidene difluoride (PVDF).

The substrates used were various aluminium laminates such as Al/PET, Al/paper and Al/paperboard as well as all metallic titanium coated aluminium foil. These all are valid alternatives for practical components.

The electrolytes were applied as liquid, gel or bound to polymers. Aqueous, organic and ionic liquid (IL) electrolytes were used. The salts tested in aqueous electrolytes were NaCl, $NaNO_3$ and Na_2SO_4. As organic electrolyte the only alternative was 0.5 M tetraethyl ammonium tetrafluoroborate in propylene carbonate which was preferred to acetonitrile because of environmental reasons.

Several ionic liquids (IL) based on organic electrolytes were used, and especially new environmentally friendly ILs were shown to work well in combination with the Chitosan/activated carbon electrodes. Clear life time related improvements in the case of using Ecoeng 212 electrolytes were achieved and of the environmentally friendly ILs, two showed very little aging problems and can be a viable alternative in safe/environmentally friendly SCs. A publication on this was submitted.

The possibility to make solid electrolytes, membranes and gels of these was investigated. Supercapacitors using e-beam curing to make the solid electrolyte were realized. Due to interaction of the monomers with the activated carbon electrodes these have lower performance (1/10 of normal capacitance values) but might be usable in applications where this is not crucial.

A new and simpler device layout, a lateral supercapacitor, was printed and promises to be a cheap and easy to manufacture solution to low power applications. The lateral SCs manufactured by screen printing had roughly 1/5 of the capacitance and 1/10 of the maximum power of a face-to-face assembled supercapacitor occupying the same area.

The basic structure of the supercapacitor cells was designed to be applicable both in small and large scale components. Supercapacitors were manufactured both in laboratory and pilot scale. Six pilot scale roll-to-roll experiments were done. They gave large amount of practical

data of the printability of the inks and the required process parameters such as printing speed and furnace temperatures. The pilot experiments showed that the production by printing is feasible. Further work is needed to develop the materials and optimize the process parameters. The printing properties of inks including long drying time requirements are not yet completely ready for the needs of flexible fabrication of supercapacitors in production scale.

Basically two different sizes of printed supercapacitors were made. In the smaller layout the geometrical electrode area was about 3-4 cm^2 and in the larger layout about 100 cm^2. Depending on the electrode thickness and electrolyte, typical capacitance values for these were 0.1-0.5 F and 5-20 F, respectively. Efficiencies above 90 % were typical for supercapacitors with aqueous or organic electrolytes. The higher ionic resistance typical for IL electrolytes resulted to lower efficiencies of 75 – 90 %. By cyclic charge-discharge experiments it was shown that the performance of the manufactured supercapacitors remains almost constant for 50000-100000 cycles.

Life cycle analysis (LCA) was conducted from a manufacturing, use and disposability point of view.

The developed supercapacitors were used in various demonstrations. They were applied as hybrid systems together with photovoltaic cells to supply the power needed in active RIFD tags. Supercapacitors with organic and IL electrolytes were used in this demonstration. Due to the requirement of low leakage current in both cases series connected supercapacitors were used even if the voltage range of a single component would have been adequate. The larger demonstration was a supercapacitor pack to drive an electric motor. A set of supercapacitors with organic electrolyte and 112 cm^2 geometrical electrode areas was used in this demonstration.

As a benchmark a commercially available lithium ion capacitor from JSR Micro was characterized and found to have electrical properties in accordance with the specifications given by the manufacturer.

Contents

1. Introduction

The aim of the project was to facilitate supercapacitor manufacturing process by printing technology. This enables low-cost manufacturing process that is important in order to widen the application range of supercapacitors. Another significant advantage is the ability to design energy storage components of required physical shape. Since the focus of the project was in the development of inexpensive alternatives, activated carbon and manganese oxide electrodes were used. The electrolytes were applied as such, as gel or bound to polymers. The basic structure of the supercapacitor cells was designed to be applicable both in small and large scale components.

Conventionally supercapacitors (=ultracapacitor, electric double layer capacitor, EDLC) are separate components used in applications where relatively high peak power is needed, such as in vehicles and wind power plants. However, smaller supercapacitors have also been developed and are now widely applied e.g. in memory back-ups. The power density (kW/kg) of the supercapacitors is typically 10-fold compared with Li-ion batteries. Analogously the charge time of a supercapacitor can be of the order of few seconds. The cycle life of a supercapacitor can exceed 1 000 000 cycles which is superior to battery cycle life of 500 – 3000 cycles. The drawback of supercapacitors compared to batteries is that the energy density is considerably lower, only 10 % of the energy density typical to Li-ion batteries. In practical applications the cycle period of supercapacitor systems is normally from about one second to about one minute.

Targets:

The participating companies can use the project results both in manufacturing supercapacitors and their materials, as well as in supercapacitor applications. The development work facilitates the tailoring of supercapacitors to various applications. The basic material choice can be applied both in small and large scale components. The layout and structure depend on the required energy and power levels. The supercapacitor development work included the optimization of capacitor properties such as capacitance, series resistance and leakage current.

The project was structured to work packages in the following way:

WP1 Electrode materials
- Activated carbon was used as the anode electrode material. The use of lignin (VTT) and nanocellulose to produce the activated carbon minimizes the material costs and environmental influences.
- Manganese oxide was used as the cathode active material together with activated carbon anode. By using this kind of asymmetric structure the capacitance is increased and also the maximum voltage with aqueous electrolytes can be increased to about 2 V. Carbon nanotubes were added to manganese oxide to optimize electric properties.
- Chitosan, PVDF and cellulose were used as binder materials for activated carbon and manganese dioxide.
- Development of printable formulations of electrode materials
- Structural characterization of the materials: SEM, X-ray diffraction

WP2 Electrolytes
- The electrolytes were in liquid state, in gel-form or bound to polymers to make a "solid state" supercapacitor. This facilitates the manufacturing process by printing

      methods. Also the safety of the components is improved since the risk of leakage is decreased.

- The gel (e.g. polyethylene oxide) or polymer matrix (e.g. PVDF) can contain either aqueous or organic electrolyte depending on the capacitance, voltage and safety requirements.
- The "solid" electrolyte makes the separator unnecessary and thus makes the supercapacitor manufacturing easier.
- Characterisation by impedance spectroscopy and FTIR

WP3 Printing of electrodes and electrolytes

- Electrode ink printing experiments (materials from WP1)
- Electrolyte ink printing experiments (materials from WP2)
- Characterisation of printed layers, surfaces and interfaces: optical microscopy, stylus profilometer, white light interferometer, conductivity
- Electrochemical characterization of printed structures: voltammetry

WP4 Supercapacitor manufacturing

- Capacitor structure and fabrication concept design
- Development of solutions for encapsulation and packaging. Alternatives included lamination and sealing inside a foil envelope
- Fabrication of supercapacitor prototypes of various sizes and shapes
- Component level electrical characterization (capacitance, leakage current, series resistance)
- Industrial experiments
- LCA considerations

WP5 Demonstrations

- Exploring possible applications, one or more of which may be chosen to be realized as demonstration devices
- Design, assembly, characterization and demonstration of the chosen demonstration devices

2. WP1 Electrode materials

2.1 Activated carbon electrodes

2.1.1 Standard electrode structure

Al/PET, Al/paperboard laminates and titanium coated aluminium foils were used as substrate for electrodes. The substrates and their properties as well as the structure of the supercapacitor are described in WP4/chapter 5.

Applying a graphite layer on the aluminium current collector has two functions. The layer protects the metal from corrosion in the case of aqueous electrolyte and on the other hand it decreases the contact resistance between metal and activated carbon layer.

The activated carbon ink used in the experiments was the same that was developed in earlier project using chitosan as a binder. For supercapacitors with organic electrolyte also carboxymethyl cellulose and PVDF binders were used. The activated carbon ink was applied either with bar coater (laboratory scale) or by screen print (pilot scale). Both methods resulted in reasonably smooth surface quality. In the experiments the geometrical activated carbon layer area varied from 3 to 112 cm^2.

The drying time of the activated carbon layer is about 10 minutes at 23 ^{o}C and about 1 minute at 50 ^{o}C.

2.1.2 Carbon synthesis

The hydrothermal carbonization (HTC) process was used to convert lignin into high surface area carbon. The lignin was obtained from kraft pulping process (HW). The HTC process was carried out in a 500 mL reactor rotating in an air-heated oven.

Carbon materials from VTT manufactured by the HTC process were characterized at ÅA utilizing both scanning electron microscopy (SEM) techniques in conjunction with elemental analysis (Energy Dispersive X-Ray Analysis EDXA) and thermogravimetrical (TGA) methods utilizing qualitative emission gas analysis. Both lignin- and sucrose-based carbon materials were characterized with the main focus on the elemental composition and thus the degree of carbonization.

The HTC process conditions in Batch 1 (Fig 2.1) were 200 °C or 220 °C and pH 7. The reaction time was 6 hours. In Batch 2 (Fig 2.2), the HTC treatment was preceded by refining the lignin in a Masuko mill (4 loops), to homogenize the lignin and keep the carbon particles small and uniform in size. The resulting carbon product from Batch 2 seemed to match the expectations of having a smaller particle size, but the problem with both batches was the strong presence of kraft black liquor, which has a negative impact on the conductivity and therefore makes it difficult to prepare the SEM images.

ÅA results   **VTT results**
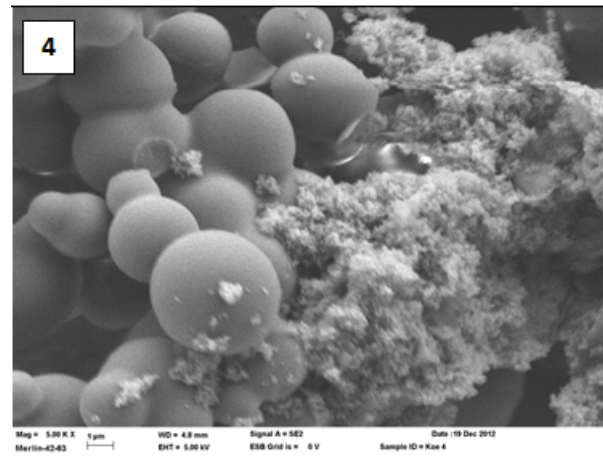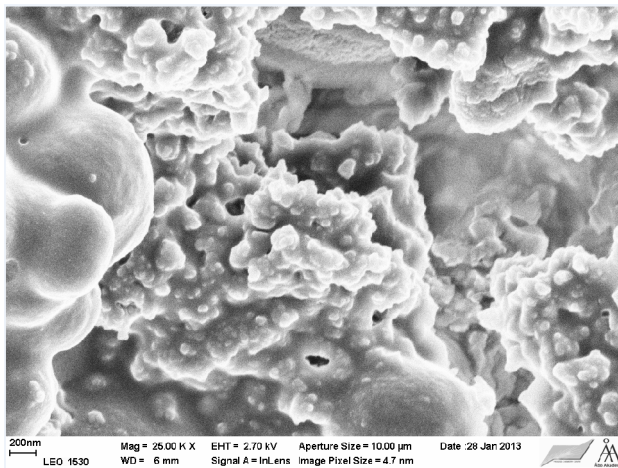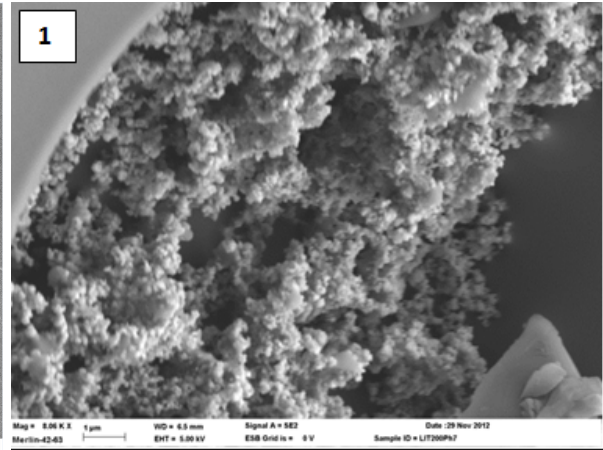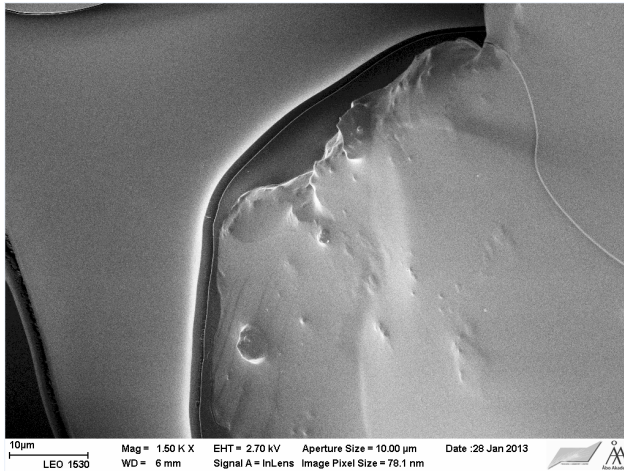
Element	Sample 1 BL lign, T200 pH 7	Sample 4 BL lign, T220 pH 7
C, %	86.4	79.9
O, %	12.1	18.8
S, %	1.2	1.3

Figure 2.1. Batch 1.

ǍA results
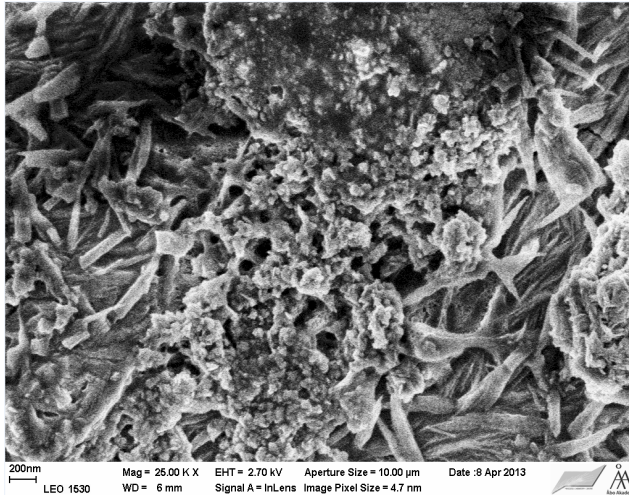
Element	Sample BL-kol 30x (1)
C, %	32.1
O, %	46,5
Na, %	19.7
S, %	1.6

Figure 2.2. Batch 2.

Lignin-based carbon samples showed typically elemental composition of some 60 % (by weight) of carbon, 35 % oxygen, 1.5-2% sulphur and remaining traces of sodium and aluminium (hydrogen is not detectable in EDXA). Improved washing of the sample reduced the sodium and oxygen contents of the samples, although the sulphur content did not reduce. The high oxygen (35 %) content was a clear indication that the hemicellulose in the precursor material was not completely thermally decomposed and carbonized. The sulphur and sodium seemed to be chemically bound to the carbon material, as they couldn't be completely removed by the thorough many-stage washing process.

The thermal behaviour of the lignin-based carbon material was characterized by DSC- MS (Differential Scanning Calorimetry, Mass Spectrometry) in nitrogen atmosphere. The coupled MS equipment was utilized to identify the emitted gaseous thermal decomposition products from the DSC in real-time and synchronized to the actual sample temperature. The results supported the elemental analysis data, that the samples were incompletely carbonized hydrocarbons with substantial traces of sulphur.
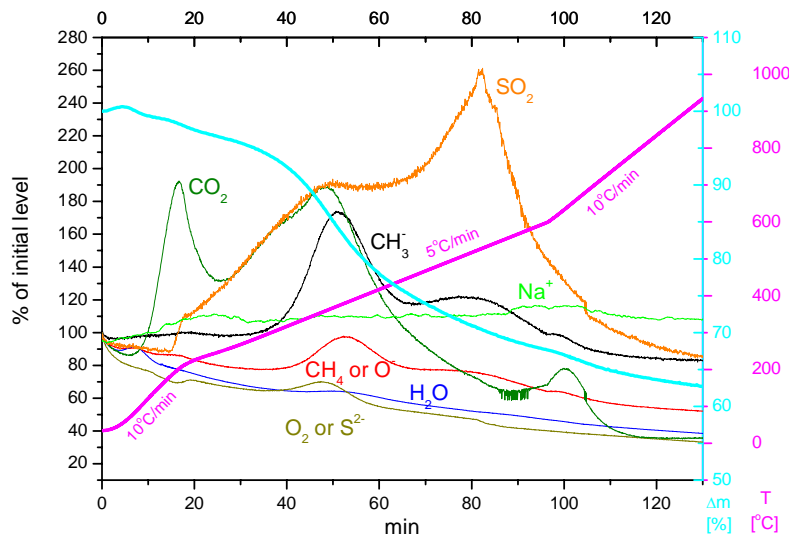
Figure 2.3. DSC-MS curves of lignin-based HTC carbon.

A DSC-MS graph is shown in 2.3. As can be seen in the curves, in this measurement typical hydrocarbon thermal decomposition fragments (CO_2, CH_3^-) were present. SO_2 was also emitted, which confirms the presence of sulphur and oxygen in the sample. The sample mass, shown as the cyan-coloured legend, is reduced to some 62% of the original mass. This further indicates the presence of incompletely decomposed precursor material.

The sucrose based carbons showed in general a better degree of carbonization than for the corresponding lignin based carbon materials. As the precursor material is a pure hydrocarbon, no trace elements were expected in the elemental analysis. The EDXA for the sample however, showed a significant amount of silicon (in the form of silica), the origin of which was unclear. The current interpretation is that the silica is dissolved from the glass during the chemical activation of the carbon material, which is performed at high temperature together with solid KOH, which is known to corrode glass (silicate) materials. A SEM image showing the silica contamination in sucrose based HTC carbon is shown in Figure 2.4.
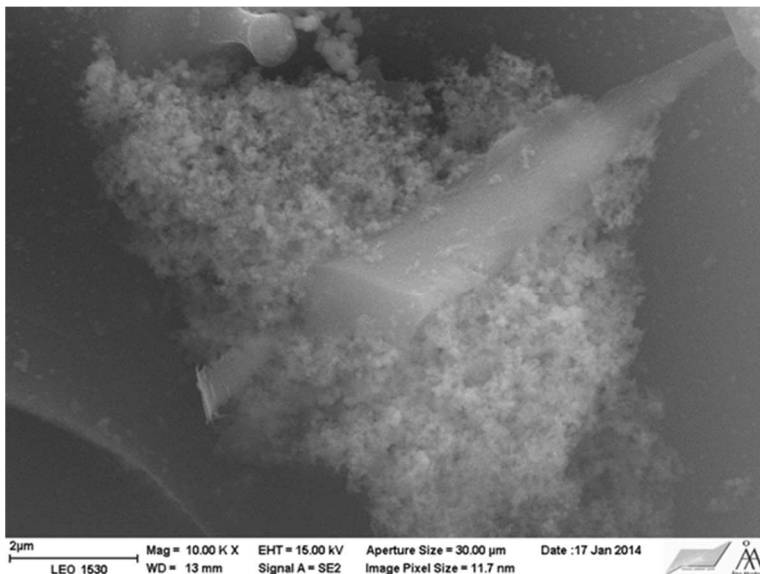

Figure 2.4. SEM image of silica contamination in HTC carbon taken at 10000× magnification.

Elemental analysis of the sucrose based carbon showed typically a composition of some 75 % carbon, 20 % oxygen and 5% silicon. Taking the atomic masses into account, these values give a (molar) ratio of Si and O to 1:6, which is clearly higher than the 1:2 expected in silica (SiO_2), thus indicating that some oxygen is still bound to the carbon material.

The DSC-MS measurements showed a manufacturing-batch dependent degree of mass loss ranging from a few to nearly 20 %, combined with clear indications of emitted hydrocarbon decomposition fragments. Further, SEM imaging also showed a large difference in sample morphology between the batches, which is a clear indication of inconsistencies/differences during treatment.

In a final attempt to improve the quality of the carbon, a chemical activation was carried out using KOH as the activating agent. The activation was done on two samples, a sucrose and a kraft lignin carbon produced by HTC (200°C). The samples were mixed with dry KOH in a mortar and activated for 1h at 700°C in a horizontal furnace under nitrogen gas flow. Then the samples were washed with 10% HCl and deionized water to remove inorganic material. Finally the samples were dried overnight at 120°C, prior to analysis. The SEM/EDX results are shown for lignin in Figure 2.5 and for sucrose in Figure 2.6.

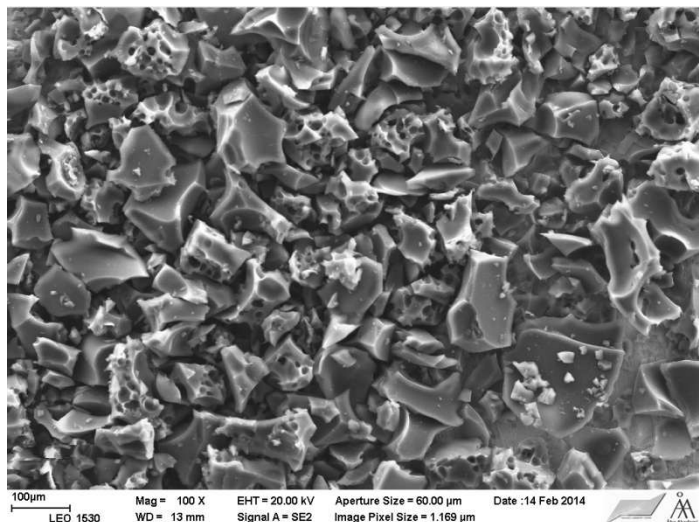| Element Line	Element Wt.%	Wt.% Error	Atom %
C K	98.25	±2.52	99.36
S K	1.13	±0.07	0.43
Cl K	0.62	±0.08	0.21
	----------		----------
Total	100.00		100.00

Figure 2.5. SEM/EDXA image and results for chemically activated HTC carbon from kraft lignin.

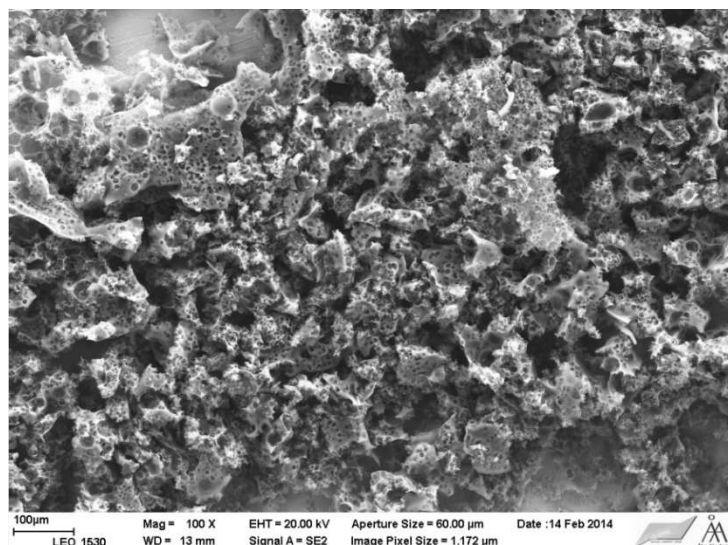| Element Line	Element Wt.%	Wt.% Error	Atom %
C	98.79	±2.53	99.53
Si	0.52	±0.03	0.22
S	0.18	±0.03	0.07
Cl	0.52	±0.03	0.18
	----------		----------
Total	100.00		100.00

Figure 2.6. SEM/EDXA image and results for chemically activated HTC carbon from sucrose.

Both samples have a high content of carbon, whereas the sample made from sucrose contains less sulphur (0.52%) compared with the kraft lignin sample (1.13%), which may affect the performance of the carbon in a capacitor application. The result is encouraging, as it shows that HTC in combination with chemical activation can produce a pure carbon from different raw materials. A disadvantage with the chemical activation process is that the overall carbon yield is very low and varied from batch to batch. More work would be needed to optimize the activation process.

Cyclic voltammetry was used to measure the electrochemical properties of sucrose based activated HTC carbon. Due to relatively high resistance the scanning speed was kept low. The curves are shown in figure 2.7. The capacitance increased also as a function of time indicating that the pores are wetting quite slowly. On the basis of CV data the specific capacitance for this carbon is about 65 F/g.
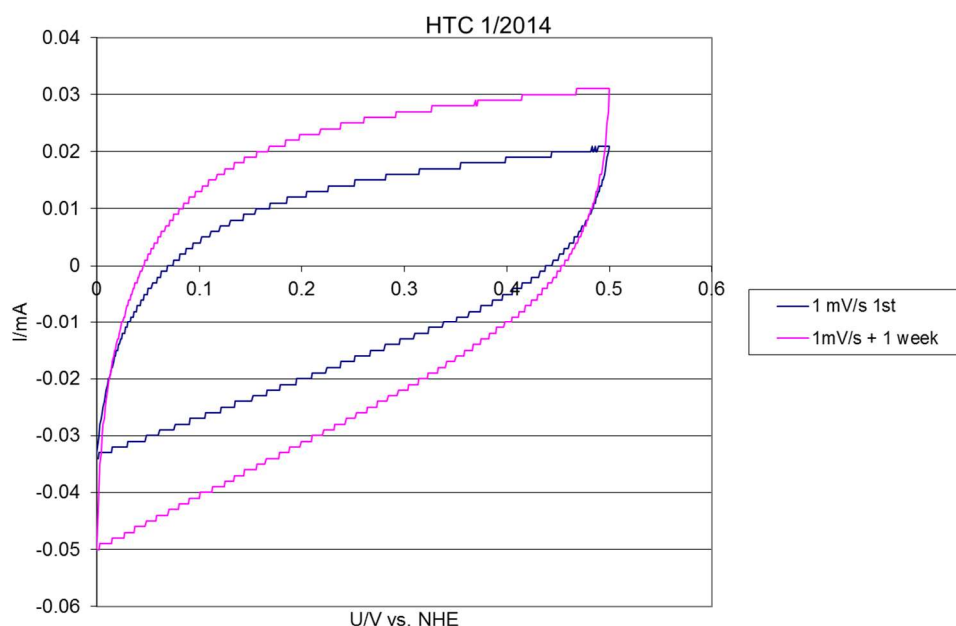

Figure 2.7. Cyclic voltammetry for HTC processed activated carbon made of sucrose.

2.1.3   Manganese oxide electrode

Sol-gel method was chosen as the approach for preparing manganese dioxide (MnO_2) for the electrode ink. Initially the synthesis produced mixed oxides with undesired oxidation states of manganese, but with an additional nitric acid treatment the oxidation state of manganese could be raised up to the desired +IV. This synthesis method is reported by Hashemzadeh et al. 2009[1]. The method is quite simple, water-based and does not involve any hazardous chemicals. It also seems to be reproducible in terms of giving the desired oxidation state of manganese. This was verified by X-ray diffraction (XRD).

---

[1] Hashemzadeh, F., Mehdi Kashani Motlagh, M., & Maghsoudipour, A. (2009). A comparative study of hydrothermal and sol–gel methods in the synthesis of MnO2 nanostructures. *Journal of Sol-Gel Science and Technology*, *51*(2).

Energy dispersive X-ray spectroscopy (EDX) was used to find out the atomic percentage of each chemical element present in the sample. EDX was run with scanning electron microscopy (SEM) at Åbo Akademi. The following SEM images and EDX data were drawn from a self-synthesized MnO_2 sample labelled as PRS006 and a commercial MnO_2 sample from NOAH technologies.

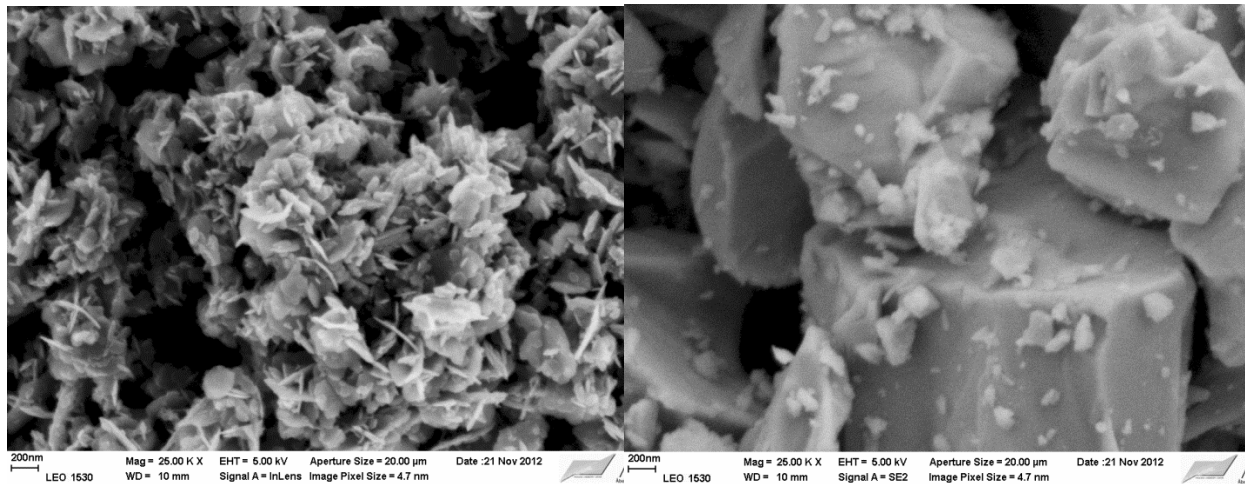Figure 2.8. SEM images of MnO_2 samples with same magnification. Left: Self-synthesized MnO_2 sample PRS006. Right: Commercial MnO_2 product from NOAH technologies.

PRS006 seems to consist of nanoscale flakes, which is advantageous for the surface area. On the contrary, the surface area of the commercial MnO_2 product seems to be quite low. BET surface area measurements will be conducted on suitable samples to verify the differences in surface area and especially its linkage to the electrochemical performance.

Table 2.1. EDX results from MnO_2 samples.

Sample	O (atom-%)	Mn (atom-%)
PRS006	65.48	34.52
NOAH	59.41	40.59

The atomic percentage of elements shows that in PRS006 the ratio between manganese and oxygen is the desired 1:2, which produces MnO_2. On the other hand, the commercial product consists of manganese and oxygen in ratio 2:3, which implies compound Mn_2O_3. This is in contrast with the XRD data recorded for the same sample, as can be seen in the next figure.
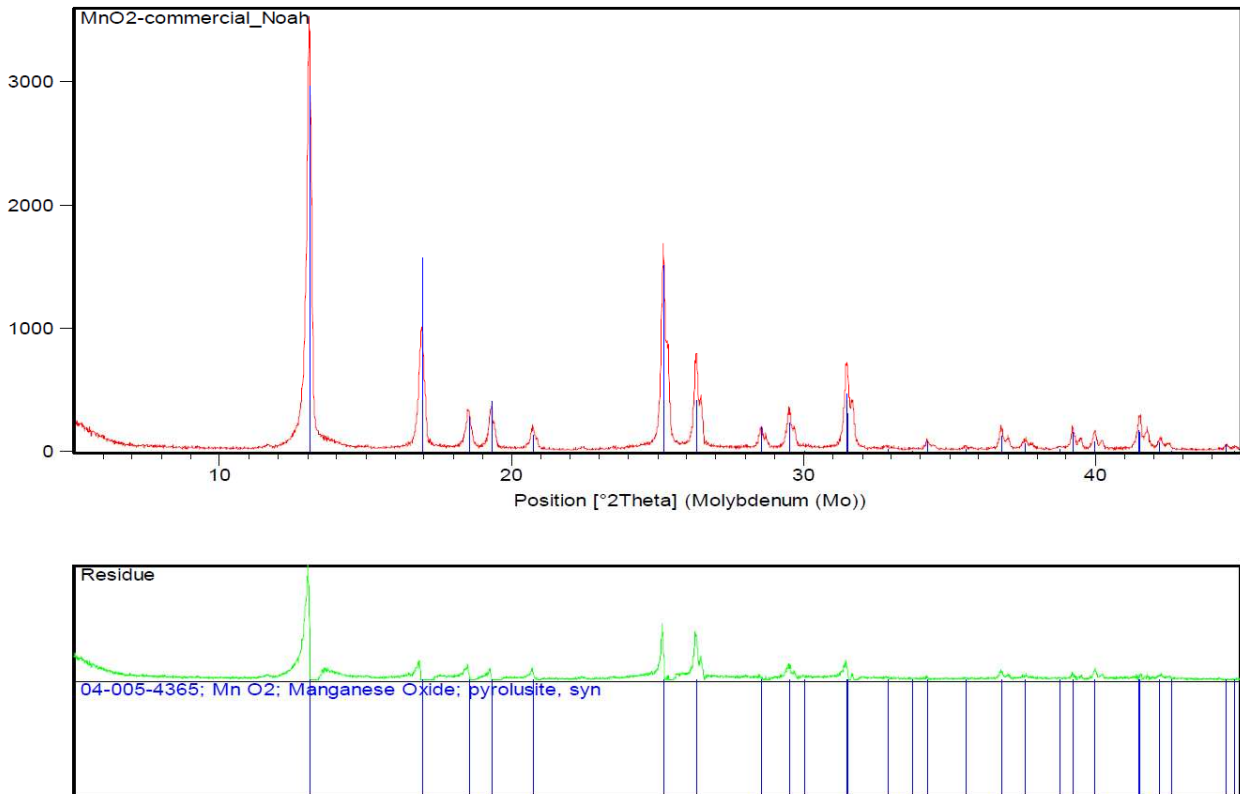
Figure 2.9. XRD curve of the commercial MnO₂ sample. XRD shows only one crystalline oxidation state of manganese, which is different from the EDX results.

The different results from XRD and EDX could not be fully explained. One reason might be, because XRD only detects crystalline phases, that the material partly consists of other oxidation states with amorphous nature.

The target batch size has been increased from a few grams to 10 grams, although mass loss occurring during the acid treatment/neutralization step of the procedure lowers the actual yield by few grams. It is possible that during the acid treatment the manganese product undergoes oxidation states that are water or nitric acid soluble. Part of the material is also lost during the neutralization by filtering.

Varying acid treatment conditions were tested in order to see if the conditions affect the oxidation state of manganese. The conditions were:

A) 2 M nitric acid, 2 h , 80 °C - the normally used conditions

B) 4 M nitric acid, 2 h, 80 °C

C) 2 M nitric acid, 2 h, 100 °C

According to the XRD, figure 2.10, the differing conditions did not have an effect on the oxidation state of the crystalline species.
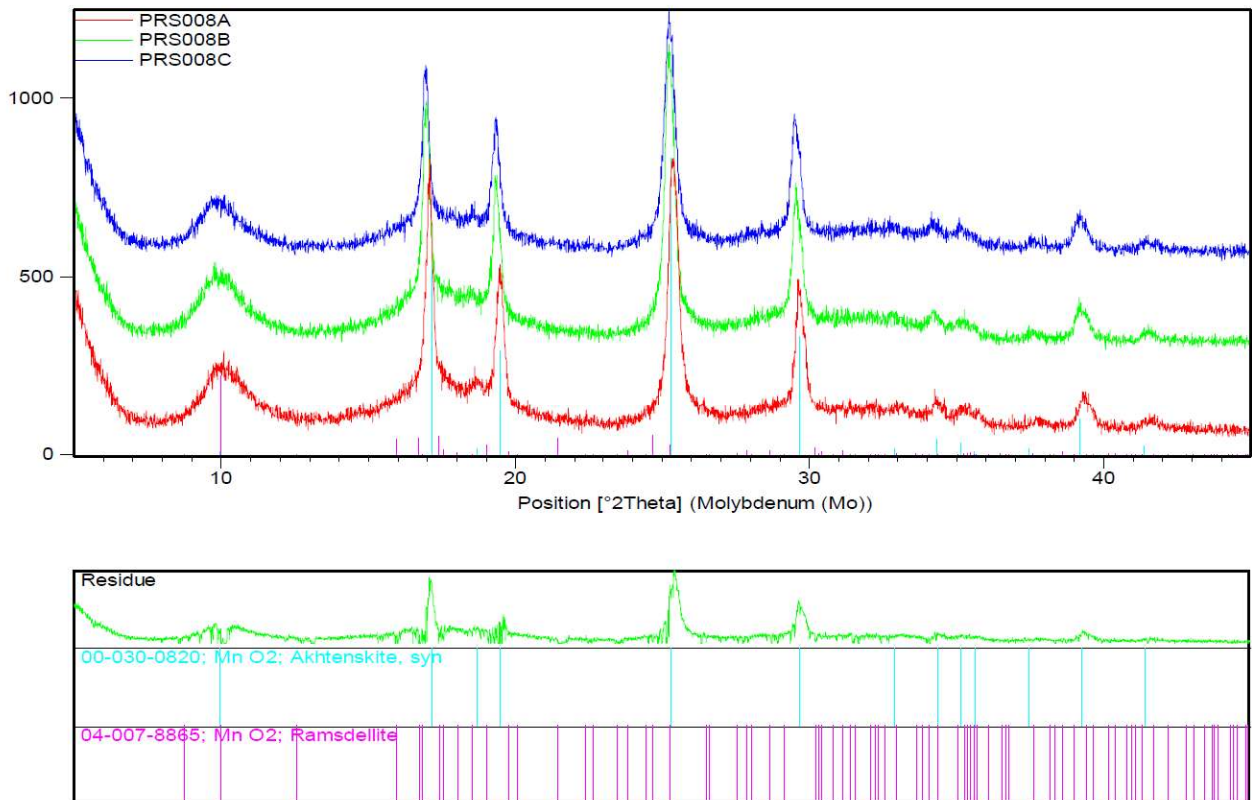
Figure 2.10. XRD spectra of PRS008 samples acid-treated in different conditions do not reveal any differences in the crystalline oxidation states.

In addition to the self-synthesized MnO_2, a batch of MnO_2 was also manufactured by mechanical processing in a ball mill. Commercial MnO_2 from NOAH was used as a raw material. The mechanical processing is a potential method in producing nanostructured material with a high specific surface area. To improve the electrical conductivity, carbon was added to MnO_2 in the milling process.

The electrochemical activity and capacitance of MnO_2/CNT composite samples were tested in a half-cell construction. At best these showed single electrode specific capacitance values in the range of 200 – 300 F/g.

In the second synthesis phase (samples called PRSTM) MnO_2 nanopowders were prepared by sol-gel synthesis from manganese acetate and citric acid. The use of citric acid was the major change compared with earlier experiments. Ammonia was added to adjust pH to 6 and a wet gel was obtained by heating at 80 $^{\circ}$C. The gel was calcined by heating at 380 $^{\circ}$C. The calcined product was oxidised by treatment with 2M or 4M sulphuric acid and washed with water. Brownish-black manganese dioxide was obtained. The crystalline structures were identified by powder X-ray diffraction. Two different crystalline phases were obtained depending on the duration of calcination step.

At ÅA the synthesized MnO_2 materials were characterized utilizing electrochemical and SEM techniques. Electrochemical measurements were performed both with pure powders and with self-assembled components. Both chronoamperometry (CA) and cyclic voltammetry (CV) were utilized.

CA and CV methods indicate that the increased operational voltage window of 2 V for aqueous electrolytes was not achieved. The aqueous electrolyte in contact with the MnO_2 material is "pseudo stable" above the thermodynamical dissociation limit for water of 1.23V, but the apparent shorter term stability is only due to kinetic limitations of the water

dissociation process. The effect was clearly seen when polarizing the material up to 2V, which was the project-set target. At already 1.5 V oxygen radicals (or peroxide) start to form, and were detectable by rotating ring-disk electrode (RRDE) experiments. The literature information of the possibility to use a supercapacitor with asymmetric structure having MnO_2 cathode was thus found to be slightly misleading from practical point of view. The higher voltage would require an application where the supercapacitor is continuously charged and discharged thus avoiding longer term use at constant voltage above about 1.3 V.

Elemental analysis was performed by EDXA on the synthesised powders, showing oxygen/manganese ratios of roughly 1.95 – 1.8, thus indicating that the manganese oxide did not consist of pure MnO_2, but also partly of other manganese oxides. This was also suspected based on the electrochemical response of the material during potential cycling, as a slowly disappearing oxidation peak indicated a transformation of the material during polarization.

A DSC measurement was also performed for the VTT synthesized PRSTM1 manganese oxide sample in nitrogen ambient. Up to some 550 °C, a roughly 10 % mass loss was observed, which corresponds well to (β) MnO_2, which has a thermal decomposition temperature of 535 °C. The 10% weight loss also corresponds well with almost pure MnO_2, assuming the thermal decomposition reaction $4\ MnO_2 \rightarrow 2\ Mn_2O_3 + O_2$. Presently the slightly contradictory observations when comparing EDXA and electrochemical results with DSC results cannot be fully explained.

PRSTM1 and PRSTM2 MnO_2 samples were applied on graphite foil and titanium coated aluminium foil to be tested by CV method also at Fraunhofer institute (IKTS, Dresden). For the majority of the coated samples reliable results were not obtained due to too thick MnO_2 layer resulting to high resistance. However, for a thin part of a PRSTM1 single electrode sample a specific capacitance of about 600 F/g was obtained.

3. WP2 Electrolytes

3.1   Conventional electrolytes

Conventional salt/solvent electrolytes in combination with the VTT-printed activated carbon based SC electrode structures were studied. Different aqueous and organic solvent based electrolytes were investigated and their intrinsic advantages and drawbacks were assessed.

3.1.1   Aqueous electrolytes

In the beginning of the project, the aqueous electrolyte of choice was a 3.4 M solution of sodium chloride (mass ratio 1:5) in de-ionized water, mainly due to its very low price and its non-toxicity and compatibility with, for example, food packaging. The sodium chloride electrolyte also exhibit good ion conductivity and low-temperature behaviour, which are beneficial for the operation of the supercapacitor component.

As alternatives to NaCl also Na_2SO_4 and $NaNO_3$ salts were used in aqueous electrodes. The results of these when applied in supercapacitors are reviewed in chapter 5.

3.1.2   Organic electrolytes

The benchmark organic electrolyte was chosen to be $TEABF_4$ in acetonitrile, a well-established commercially utilized combination in supercapacitors. The $TEABF_4$ concentration in all measurements was 0.5M, despite that the maximum solubility of the salt in acetonitrile is about 1M. Previous measurements have shown that the capacitance obtained with this concentration is close to that of the almost saturated 1M solution and the reason for using the lower concentration in the experiments is to minimize both the electrolyte cost and the risk of precipitation due to solvent evaporation during the experiments.

Measurements have also been performed with $LiBF_4$ as salt, a cheaper and less hygroscopic alternative to $TEABF_4$, also dissolvable and dissociating in acetonitrile. In previous projects a favourable synergy has been found between the combination of $LiBF_4$ and $TEABF_4$ dissolved in acetonitrile in combination with activated carbon powders. The increase in capacitance has previously been determined to some 15% as compared with the corresponding pure salts when using a 50:50 molar ratio of the salts. The synergetic effect has only been seen for mesoporous materials and the probable explanation is an improved packing efficiency of the different ionic species in the electrical double layer of the electrode structure. The hypothesis is that steric and electrostatic repulsive forces limit the TEA^+-ion packing within the smaller pores of the carbon. The smaller-in-size Li^+-ions experience smaller repulsive hinders within the pores and can thus utilize parts of the surface area within the pores unreachable for TEA^+, thus effectively increasing the active available surface area of the electrode structure. The possible intercalation of Li^+ into the carbon structure is acknowledged, but further studies on its possible effects have not been performed. A comparison of the performance of the aqueous vs. ACN based electrolyte is shown in Figure 3.1.
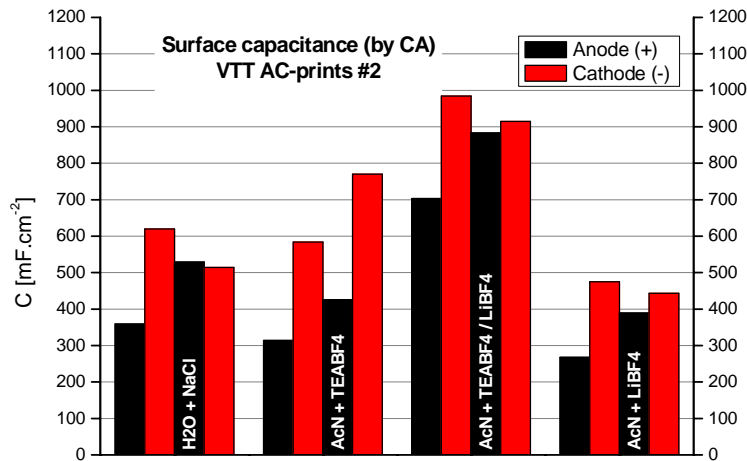
Figure 3.1. Comparison of aqueous vs. acetonitrile based electrolytes on electrode structures.

As a result of the shown synergetic effect of combining TEABF$_4$ and LiBF$_4$, a 0.25M+0.25M mixture of these salts in acetonitrile was selected as the organic electrolyte of choice.

Due to the intrinsic properties of acetonitrile, such as toxicity, evaporation, hygroscopicity and flammability, propylene carbonate as the solvent for TEABF$_4$ has also been tested. Even though the performance of the acetonitrile based electrolyte is better, propylene carbonate based electrolyte still remains as an interesting option. It should be noted, that the synergetic effect of mixing LiBF$_4$ and TEABF$_4$ has not been observed in propylene carbonate.

In the organic electrolyte supercapacitors used in demonstration 0.5 M TEABF$_4$ in propylene carbonate was used due to the toxicity difference between propylene carbonate and acetonitrile.

3.2   Gel electrolytes, PEO, PVA

Since the aim of the PRISU project was to make a printed supercapacitor structure, also the ion-conducting electrolyte layer should be printable. This can be made by using electrolytes that are in gel-form or bound to some host polymer matrix such as poly(ethylene oxide) (PEO) or poly(vinyl alcohol) (PVA). The most important characteristics of these polymer electrolytes are sufficiently high ionic conductivity as well as good thermal and mechanical properties. When the liquid phase is bound to some host polymer structure it inhibits the leakage of liquid.

The wettability of some electrolytes on the activated carbon (AC) electrode surface were tested as a function of time (Figure 3.2). It was noted that both PEO and PVA based electrolytes had good wettability on the AC electrode, since the liquid wetted the surface of 1 cm^2 in tens of seconds.

Figure 3.2. PVA based gel electrolyte wetted well the activated carbon surface.

Work concentrated on the following items :

a) Thermally crosslinkable polyvinyl alcohol (PVA) and glutaraldehyde (GA) based gel electrolyte, where hydrochloric acid (HCl) acts as the catalyser. The problem in our case was that HCl dissolves the chitosan binder of the activated carbon layer. This problem could be circumvented by a procedure, where the acidic gel is neutralized in 5M NaOH solution, then washed repeatedly and finally the neutralized matrix is immersed into mild alkaline or neutral salt solution.

b) Polyethylene oxide (PEO) based electrolytes were made having choline chloride urea (CCU) type ionic liquid as the salt component. In some samples polyacrylic acid (PAA) based superabsorbent was added to avoid early drying of the gel.

c) PEO based model solutions for viscosity measurements and inkjet printing test was made. The basic solution consisted of 1 gram of PEO (M_W = 900 000) as the host polymer in 40 ml distilled water and 0.5 gram of choline chloride urea ionic liquid as the salt. Ion conductivity value of 4.5 mS/cm was measured for this electrolyte solution, and it can be increased to 8 mS/cm by doubling the amount of ionic liquid. The molecular weight of PEO was probably too large to get a proper inkjetting results, and lower molecular weight PEO would be a better alternative.

Figure 3.3. Supercapacitor having a gel electrolyte could be charged to 1.5 V and used as a power source for a digital thermometer.

3.3   Ionic liquid electrolytes

At the FunMat center in Åbo Akademi University we have during the first year in the PRISU project had the goals of testing new electrolytes for the Super capacitors (SC). In focus has been to overcome different drawbacks with the current water and liquid based electrolytes.

- Water based electrolytes have low electrochemical window (around 1,2V) due to waters electrochemistry and prevents higher energies to be stored in the SC as power scales with the voltage squared (V^2). Ionic liquids on the other hand typically have EC windows between 4-6V (or even higher)!
- Electrochemistry of water also gives hydrogen and oxygen gas that can destroy the SC by causing bubbles and electrode de-lamination.
- Water based electrolytes as well as ILs are fluid and can easily leak out of the SC in case of puncture and therefore we also have explored solid and solidified electrolytes

To overcome these issues we have during the first year investigated the use of alterative electrolytes, such as ionic liquids (IL) and solidified electrolytes, looked at their SC behavior and possible effects from water and air. We have investigated several means of solidifying the fluid electrolytes to prevent leakages. We will here present highlights of the results including use of non-toxic ILs and e-beam curable ionic conductors. Known state of the art devices are compared to the environmentally friendly alternatives and solidified electrolytes.

During the second year we have continued with investigating the environmentally friendly alternatives and shown them to be good candidates for SCs. A manuscript partly covering the work done has been written and submitted to *Journal of Power Sources*. These SC where all manufactured with standard printing techniques. Their viscous nature makes the inner resistance usually higher than other alternatives but also prevents leakages of the electrolyte (or slows it down when punctured). The SC using these environmentally friendly electrolytes can also be charged using higher voltages (i.e. 2.5V). These SCs can be cycled several thousand times without performance degradation. The environmentally friendly ILs used in our work have been benchmark tested and compared to existing state-of-the-art ILs and organic electrolytes. A couple of particularly good alternatives were found in IL1 and IL2 that have very promising properties. A positive interaction between the IL and Chitosan was proposed as an explanation for some of the interesting results.

Lateral SCs have also been manufactured and tested. Both lateral SCs printed on PET foil and paper have been realized. The performances of the SCs are not as good as vertical devices – mainly because of the higher resistances in the electrodes (no aluminum conductor) and the higher apparent IL resistance (less cross section area). Although, both of these resistance issues can be eased by using an enhanced conductor (doubly printed carbon) or a new electrolyte approach.

3.3.1   Ionic liquid electrolytes

Two different families of ionic liquids (IL) have been tested using the VTT printed electrodes in vertical SC. The different types are (1) Imidazolium (IM) based (EMIM and BMIM) with different counter ions and (2) eutectic mixtures based on Choline chloride and different hydrogen bond donors (see Figure 3.4). The IM based ionic liquids are known to give high conducting and high capacitance devises (can be considered state of the art IL devices), but generally not considered as environmentally safe and non-toxic. Therefore also the Choline chloride base where investigated, as they are considered as non-toxic alternatives.
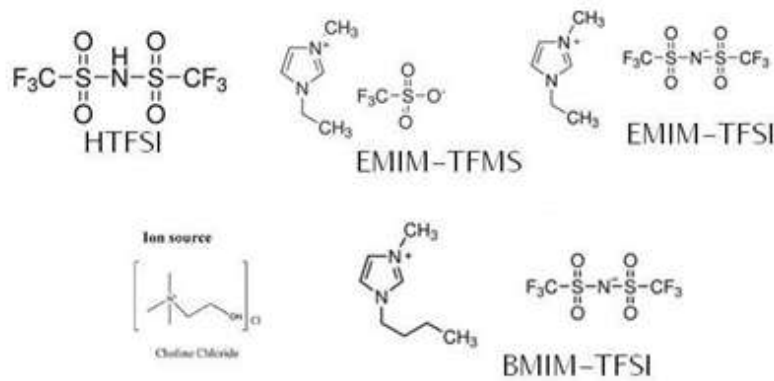
Figure 3.4. Different IL electrolytes tested at FunMat at ÅA – short names used in this report and the chemical structure shown.

The ILs have been impregnated onto VTTs printed electrodes, in a vertical setup (symmetrical areas) using o-ring separator, and characterized with impedance measurements.

From the results one can see that in general the IM based ionic liquids have higher conductivities, and this is mainly due to their lower viscosities. This is a known fact that the fluorinated ILs have lower viscosity (due to less inner friction) but also the fact that the eutectic mixtures are closer to their melting points. This makes them more viscous and hence less conducting. This could be seen from temperature dependent IS measurements on IL1.

From the CV data there can be seen that the different ILs behave rather similarly, with not very impressing electrochemical windows (even for 1,5V some unwanted EC can be seen). For the IL3 this is a demonstration of the IL3 having free protons (from the acid) that are easily reduced. For the other ILs the reason is one of the challenges with using ILs, namely their inherent property of them being extremely hygroscopic, and even the slightest contact with ambient air will render them "wet". Here no extreme care has been taken to avoid water as the electrodes have been stored in ambient, and the measurements have been performed in ambient (but ILs dried in desiccator before use).

From a summary of the electrical properties of the different ILs measured by IS and CCD one can see that the values are comparable between ordinary ILs and the eutectic mixture ILs. But one difference can be seen in the leakage current that seems to be higher for the eutectic mixtures (IL3 had even too high values). The reason for this can be either difference in water uptake and/or the eutectic mixtures having "free" protons from the hydrogen bonding moiety (or Choline chloride itself). These effects are currently being investigated, i.e. accessing the electrochemical window for the eutectic mixtures based on Choline chloride, by testing extremely dried samples (see section 3.3.2 below for initial tests).

The different ILs were investigated using impedance spectroscopy.

From the Nyqvist diagrams and capacitance and conductivity curves of the different ILs it could be seen that IL4 has the largest internal resistance and as a result the lowest conductivity and capacitance. The state-of-the-art EMIM:TFSI and the commercially available "greener" alternative ILgreenhave the lowest internal resistance and highest conductivity and capacitance. IL2, however, is not much worse and at low frequencies, the frequency at which the SC are proposed to be used, IL2 is comparable to the state-of-the-art ILs.

The different environmentally friendly ILs (i.e. the choline chloride based and ILgreen) have been made into 56cm^2 SCs. The devices were manufactured with printing technologies and laminated between plastic foils. For a summary see the attached/referenced paper.
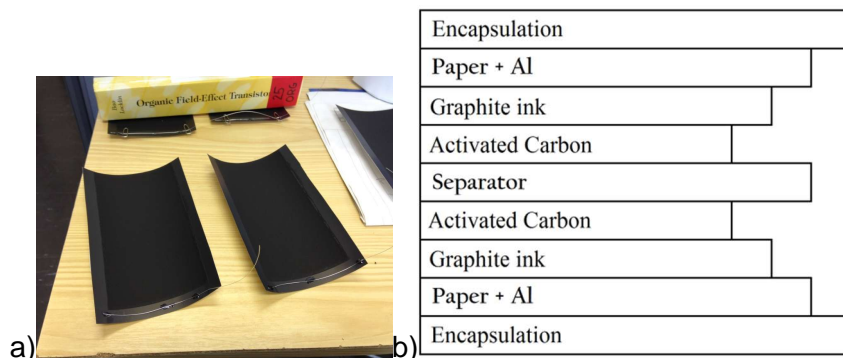

a)   b)

Figure 3.5 a) Two large area electrodes on printed on paper, b) the different layers of the 56 cm^2 printed and laminated SC devices..

From these data one can draw the conclusion that the new, choline chloride based IL devices are comparable to state of the art devices using the VTT R2R manufactured electrodes and printing deposition of electrolyte and R2R compatible lamination. For more detail on these materials and devices see the attached/referenced publication draft – "Printed environmentally friendly supercapacitors".

3.3.2   Detailed measurements on IL1 eutectic mixture

To analyse the effect of water and temperature in ILs we measured the IL1 eutectic mixture both in ambient conditions and in vacuum conditions.

Capacitance and conductivity data on IL1 showed some really interesting results as the values for the IL1 superseded those of the "state of the art" BMIM-TFSI when measured in vacuum. We analyse this data as either one of several possible effects. Firstly, the vacuum treatment can make the IL to penetrate more of the AC surface (a wetting issue) and this effect being greater for the IL1 - i.e. the higher value is due to higher surface area. Secondly, the explanation could be that as some parts of the AC prints surface is covered by the binder Chitosan, the different ILs could "penetrate" that layer differently. Due to chemical similarities between the eutectic mixtures and Chitosan (i.e. both having hydrogen bonding moieties) one could suspect that the IL1 therefore better "dissolves" in the Chitosan, and thereby reaches a larger portion of the surface area (this hypothesis is tested in section 4.2. – Printing of AC electrodes containing ILs in the ink). NOTE also that this unexpected effect of IL1 in vacuum, made it not possible to access the effect of water and find the electrochemical window of IL1. These effects/values will be measured separately in another setup, not using AC electrodes with Chitosan, and work is here ongoing (i.e. months of drying started).

A measurement of the IL1 based SC capacitance at different temperatures was made. The results are pretty clear, in that sense that at higher temperatures the lower IL viscosity gives the devices higher capacitance (roughly 10 times higher C). This finding compared with the IL1-chitosan reaction presented above, that IL1 shows promise to be a good choice as a non-toxic electrolyte, has inspired us to go further with IL1. But its high melting point (12-35 degrees depending on water level) prevents really good SC so we have initiated work of mixing IL1 with different solvents to lower its viscosity and achieve good room-temperature devices, and this work will now continue.

It seems that these new electrolytes are comparable to state-of-the-art EMIM/TFSI devices.
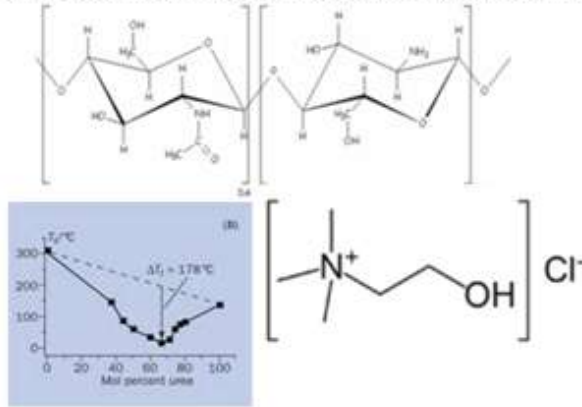
Figure 3.6. Structure of chitosan and the IL1 components and Choline chloride..

More work is needed to fully understand if this is the case. Also the SC based on IL2 behaves very nice in cycling experiments. The IL2 device actually gets better with time in the capacitance measurements, and suggested is the same explanation as above.

We have also benchmarked the state-of-the-art ionic liquid EMIM/TFSI with the usual organic electrolyte, also used in the other parts of the project – i.e. $TEABF_4$ and $LiBF_4 + TEABF_4$ in acetonitrile. This was done in order to get a grip on how good the ILs are in these R2R printed VTT electrodes.
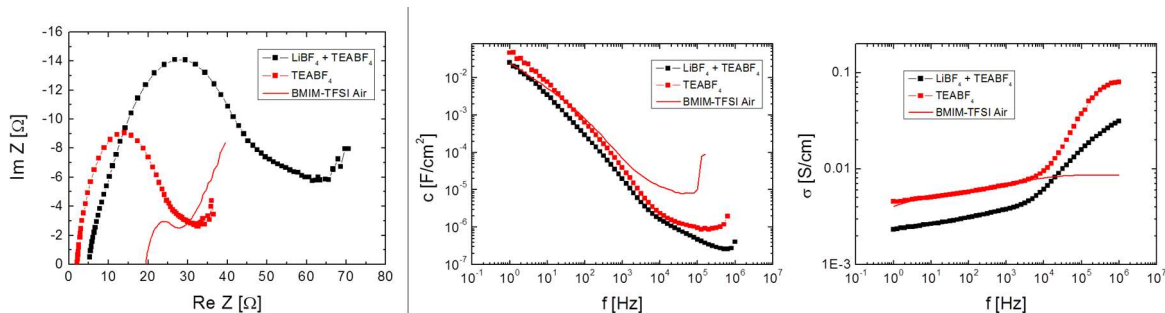

Figure 3.7. Comparison of organic acetonitrile electrolyte to the state-of-the-art electrolyte EMIM/TFSI used within our work.

The result show that the IL is very well situated as an alternative to organic electrolyte devices and also shows that all different ILs tested by us – are comparable in performance to organic electrolyte – and hence all are viable alternatives.

3.4   Lateral SCs

To be able to realize really simple and easily printable devices, the lateral electrode configuration would be an interesting choice (no need for stacking or separators). Therefore we have tested the effect of having lateral electrodes (see Figures 3.8 and 3.9).
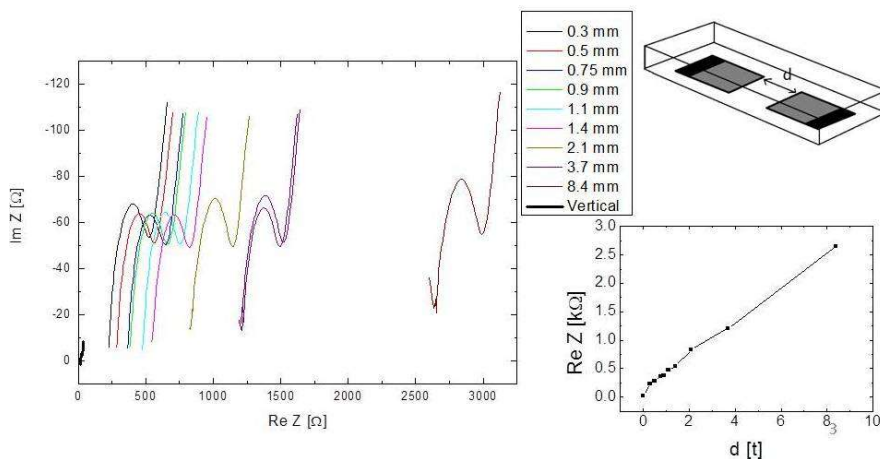
Figure 3.8. Lateral devices measured with different electrode spacings (BMIM-TFSI as the IL)

From Figure 3.8 it is clear that the internal resistance is a direct function (straight line) of the electrode spacing. This will render the lateral devices to have high(er) internal resistances than comparable vertical devices, and therefore low-current applications should be considered as they would be no good for high current applications.
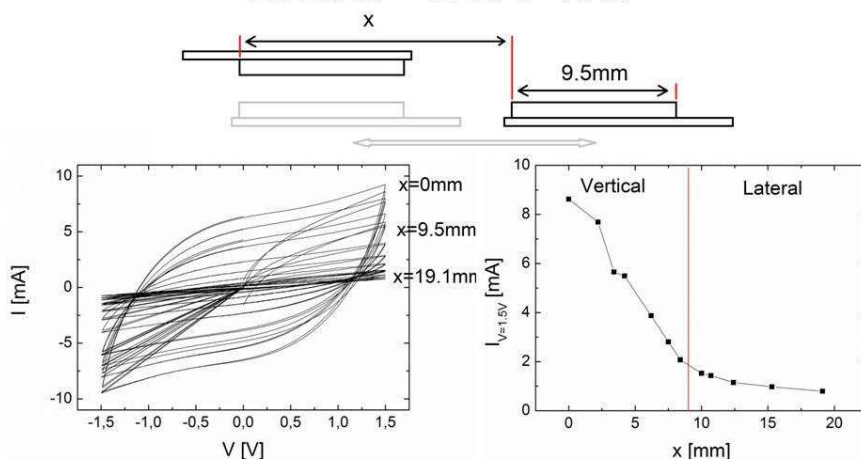

Figure 3.9. Measuring the transition region from vertical to lateral SC in an "upside down" lateral configuration.

The effect of having lateral devices compared to vertical, on the current output, can further be analysed by looking at Figure 3.9 where a transition from vertical to lateral device is measured – by displacing the electrodes gradually from each other. From this data it is clear that two separate regimes exist – vertical and lateral - and that the internal resistances as well as capacitances are much different between the two. This work is continuing by trying to affect the lateral device drawbacks (i.e. internal resistance) by using different electrode configurations (fingers, spirals etc.). This work will continue in order to optimize, and understand the nature of the lateral device in more detail.

Complete lateral devices have been manufactured using the same electrode materials as in the vertical SCs. As electrolyte in this case ILgreen was used to compare data between lateral and vertical devices.
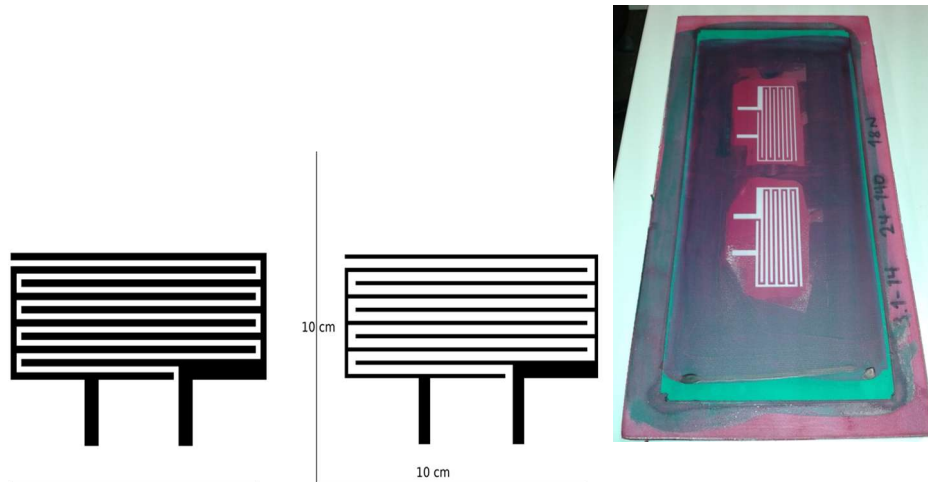

Figure 3.10. Showing lateral screen (right) and screen pattern (left) that was used in lateral printing trials. Both electrode areas (of the AC electrodes – thicker pattern) was 10 cm^2.

Devices in the first printing trials were only possible to make on paper as the PET electrodes delaminated. Filling the paper with ILgreen electrolyte and laminating gave devices that where poor in performance due to very high internal resistances – mainly due to the small amount of IL in these devices. See Figure 3.11 below.
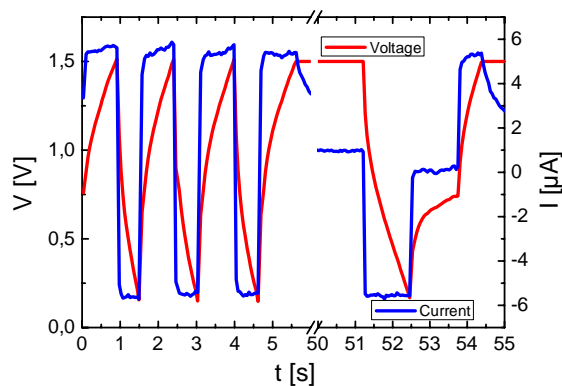

Figure 3.11. Graphite ink on PET with delaminated AC and ILgreen laminated. I = 5.6 µA (0.2 V – 1.5 V); C/A = 8.6 µF/A; I_{LEAK} = 1 µA; R_i = 94 kΩ Graphite ink on paper with AC and ILgreen laminated. Discharges faster than one step => unable to calculate internal resistance or capacitance.
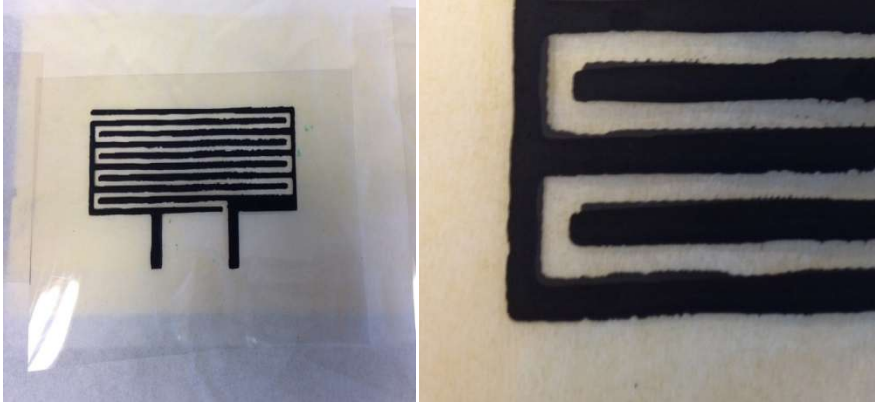
Figure 3.12. Lateral SC printed directly on paper. One layer of conducting carbon printed and covered with a printed layer of AC. ILgreen is used as the electrolyte.

3.5   Gel electrolytes and solid electrolytes

In FunMat two different approaches to achieve gelled/solid electrolytes have been tested, e-beam curing of the electrolyte and the use of polymer gelation. Some of these results are summarized here.

3.5.1   E-beam solidified electrolytes and membranes

The use of e-beam curing would be a nice way of gelling the electrolyte as the electrolyte could be supplied to the AC electrodes as a low-viscous mixture made to wet the electrodes properly, and then, after being properly distributed into all of the AC layer, cured by e-beam.
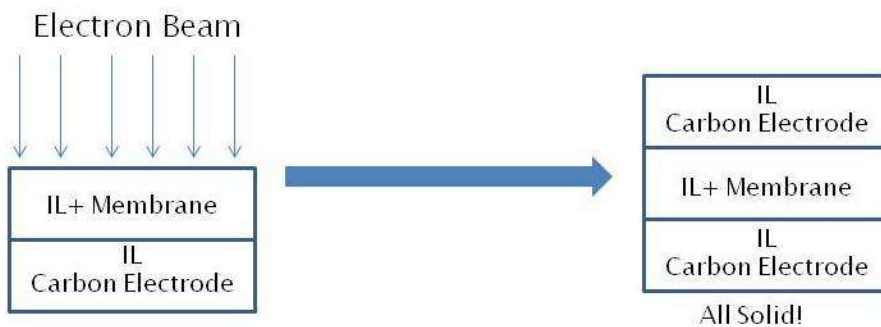

Figure 3.13. The concept of using e-beam curing to wet electrodes properly and skip the use of separator.

The use of e-beam could also make the use of separator (paper or plastic frit) obsolete as it in itself could be functioning as such. This approach was tested by making free standing membranes with e-beam curing and monomer mixtures (see Figure 3.14).

E-beam membranes – adjustable properties
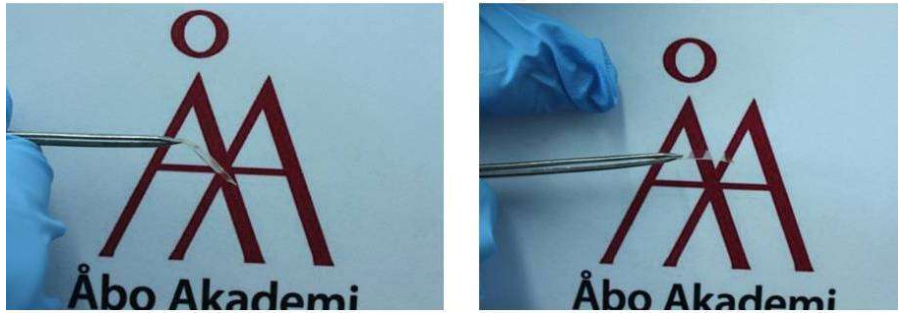
Flexible and Soft
80%IL
10% Tetra(ethylene glycol) diacrylate
10% Trimethylolpropane triacrylate

Stiff and rigid
50%IL
10% Tetra(ethylene glycol) diacrylate
40% Trimethylolpropane triacrylate

Figure 3.14. Ion conducting films/membranes made with e-beam (EMIM-TFSI IL used).

The different membranes were characterized with impedance measurement and proven to be suitable as ion conducting separators. Devices where realized where the separator used in the SC was the 80% containing IL membrane (see Figure 3.13 for setup and Figure 3.5 for measurements).

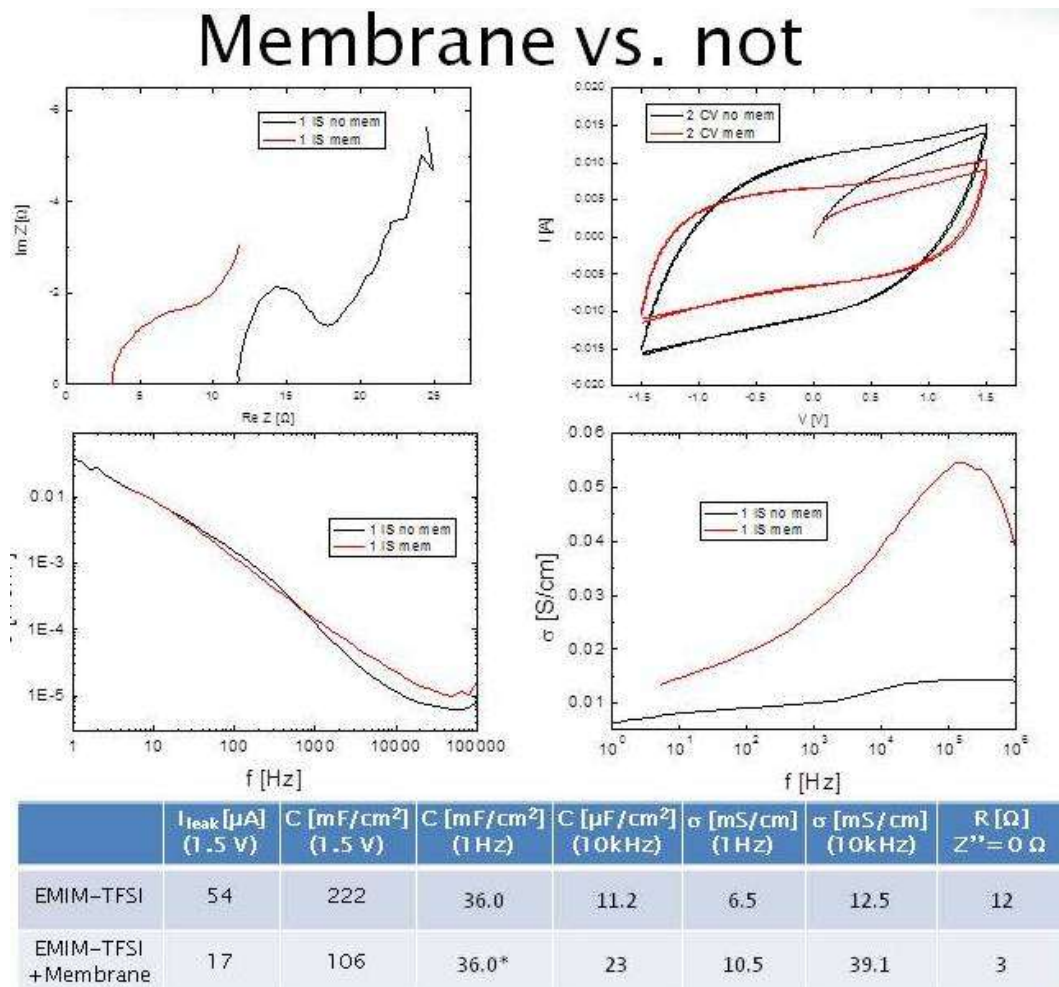|	I_{leak} [µA] (1.5 V)	C [mF/cm²] (1.5 V)	C [mF/cm²] (1 Hz)	C [µF/cm²] (10 kHz)	σ [mS/cm] (1 Hz)	σ [mS/cm] (10 kHz)	R [Ω] Z''=0 Ω
EMIM-TFSI	54	222	36.0	11.2	6.5	12.5	12
EMIM-TFSI +Membrane	17	106	36.0*	23	10.5	39.1	3

Figure 3.15. Comparison of using free standing IL membranes or not in SCs (EMIM-TFSI IL was used).

From these data one sees that the membrane adds internal resistance to the device, and shows lower capacitance values than the SC made without the membrane. This is easily

explained as the membrane restricts ionic motion and causes higher resistances. The effects where not that severe and optimization work of membranes are in progress.

3.5.2   Direct e-beam curing of IL within SC electrodes

We have also tried several formulations of ionic liquids combined with e-beam curable formulations to directly cure the whole bulk of the IL within, and above the AC to make solid electrolytes and separator layers at the same time. These results have been disappointing as the SC performance drastically dropped (100-1000 times lower C compared to only IL devices).
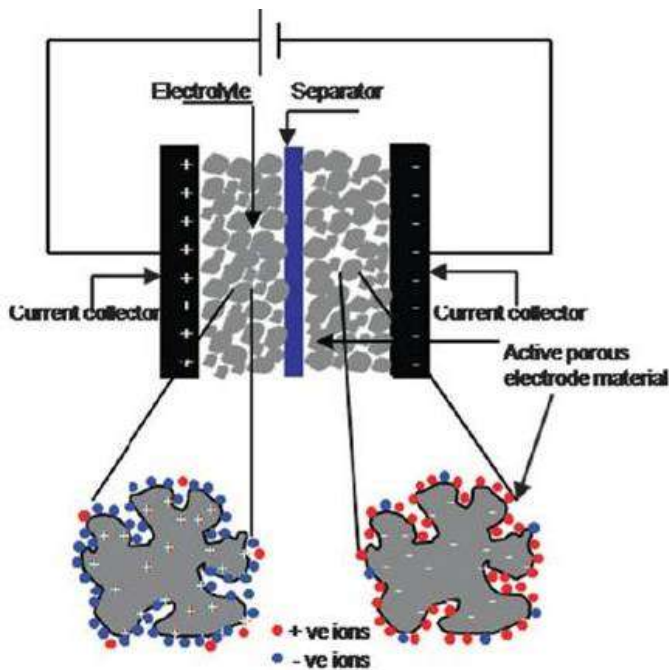

Figure 3.16. The generalized internal structure of an AC electrode SC.

This can be explained by looking at the internal build-up of these SCs (see Figure 3.16). As the bulk of the electrodes consist of active carbon (AC) the surface area is high, but it is also very "reactive" and adsorbs active molecules on its surface (known fact - as AC is used to remove organic molecules from gas streams etc.). This makes the reactive formulation supposed to cure in the e-beam, to stick to the AC surface, as it contains reactive double bond. Then when curing, more of the reactive monomers are at the AC surface, screening the surface from IL contact in the ready devices – and hence higher resistance and lower surface area devices are the result. This effect is under investigation and different routes around the problem will be tested. Among the supposed solution is to firstly "deactivate" the AC surface with non-harmful (for the capacitance and resistance) compounds that bind better than the monomer solution to the AC – and then curing. Work still in progress here.

3.5.3   Binder solidified electrolytes

Other tests with using known polymeric binders/gellators have also been conducted (see Figure 3.17). One semi-commercial triblock polymer (PS-PEO-PS) and one commercial binder system (a water PE suspension) was used in these trials.
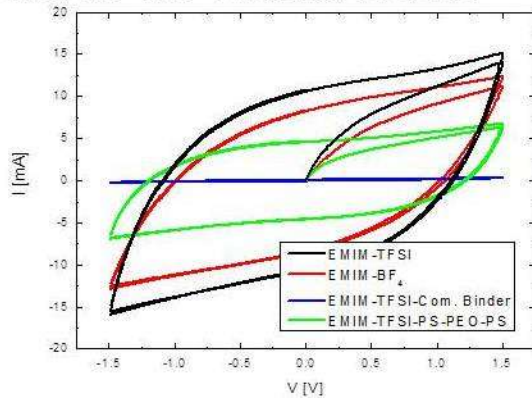
Binder in electrodes – CV

Figure 3.17. Tests with physical polymer binders (EMIM-TFSI IL used).

It can be seen that the binders affect the CV (and capacitance) values negatively. Although the triblock polymer does not affect the CV as much as the PE-suspension, and it shows promising values. The reasons for these diminishing effects can be the screening of AC surface discussed above, but it can also be related to the higher internal resistances that the gelled ILs has. Optimizations of formulations (concentration, particle sizes etc.) are currently in progress. Also new binder systems will be screened in order to find better candidates.

4. WP3 Printing of electrodes and electrolytes

.

During the project six pilot printing trials were made with rotary screen printing using VTT's ROKO pilot production line. The purpose was to manufacture electrode layers using R2R printing technologies for supercapacitors. The first printing trial was already done and reported in PEPSecond project. The main parameters of the printing trials are presented in Table 4.1. During some trials energy, substrate and ink consumption data was collected for the LCA-analysis of the supercapacitor.

Table 4.1. Main parameters of the printing trials made with ROKO.

Trial	Screen	Inks	Paper / board	Drying of graphite ink	Drying of active ink	Extra drying
1	Gallus BY (64 L/inch)	Electrodag PF-407C Norit super 30 +chitosan	SE Lunchbox	4 ovens 110°C	4 ovens 40-60°C	None
2	Gallus BY (64 L/inch)	Electrodag PF-407A Norit super 30 +chitosan	Walki C1S	2 ovens 120-140°C	2 ovens 80-90°C	Lab oven 4-10 min, 120 °C
3*	Gallus BY (64 L/inch)	Electrodag PF-407A Norit super 30 +chitosan Aquaseal X2234**	Walki C2S SE Lunchbox	4 ovens C2S: 140°C Lunchbox: 95-110°C IR + 3 ovens C2S: 5 kW + 140°C	4 ovens C2S: 140°C Lunchbox: 100°C	Lab oven C2S: 2-8 min, 120 °C Lunchbox: 15min, 100 °C
4*	Gallus BY/BZ (64 L/inch)	Electrodag PF-407A Norit super 30 +chitosan	Walki C2S SE Lunchbox	4 ovens C2S: 140°C Lunchbox: 95-110°C	4 ovens C2S: 140°C Lunchbox: 100°C	ROKO C2S : IR (5 kW) + 3x140°C Lunchbox: IR (2 kW) + 3x100°C NICO C2S and Lunchbox: IR (6x100 °C)
5*	Gallus BY (64 L/inch) Stork Prints 215V*** (215 L/inch)	Electrodag PF-407A Norit super 30 +chitosan	Walki C2S	4 ovens 90-120°C	4 ovens 90-120 °C	ROKO 4 ovens 90-120 °C
6*	Stork Prints 215V*** (215 L/inch) Gallus BY (64 L/inch)	Electrodag PF-407A Norit super 30 +chitosan	Walki C2S	4 ovens 90-100°C	4 ovens 90-100 °C	None

* The new Gallus rotary screen printing unit used
**Aquaseal layer was printed using flexography and rotary screen printing
*** Screen used only in the case of Electrodag PF-407A

4.1 Printing machine and equipment

The printing trials were made by using VTT's ROKO pilot printing machine, shown in Figure .1. Electrode materials were printed using rotary screen printing. Rotary screen printing and flexography were used to deposit the sealing material in the third trial. ROKO has four interchangeable printing units including rotary screen, flexography, gravure, and reverse gravure units. In addition, the printer consists of unwinding and re-winding units, four 1 m long hot air ovens, plasma treatment unit and possibilities for IR and UV drying. The maximum printing speed of ROKO is 10 m/min. The first one of the four dryers can be changed to IR-dryer and this option was utilised in the third and fourth printing trials. Also the

IR ovens of NICO pilot printing machine were used for the extra drying of ROKO printed samples.
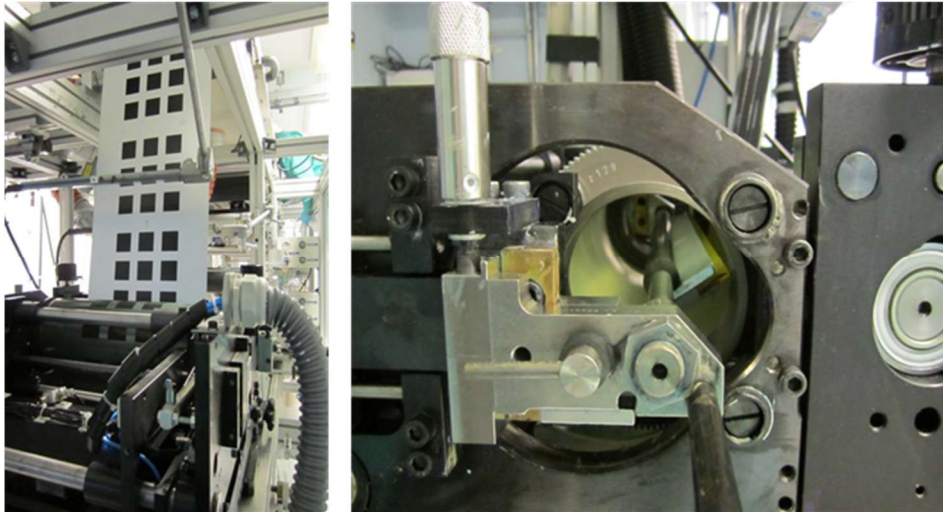

Figure 4.1. ROKO pilot-scale printing machine and screen printing unit.

4.2   Materials and methods

4.2.1   Substrates

The used substrates were aluminium (Al) coated papers and paperboard presented in Table 4.2. The aluminium coating works in this supercapacitor structure both as the current collector and barrier layer.

Table 4.2. Substrates used for the R2R printing trials.

Substrate	Thickness/ Basis weight	Al-coating thickness	Description
Stora Enso Lunchbox 240 + 12 LPDE	259 g/m^2	6-7 µm	Al-layer on the top of the paperboard
Walki C1S	80 µm	9 µm	Plastic layer between the base paper and Al-layer
Walki C2S	88 µm	9 µm	Plastic layer between the base paper and Al-layer and on the backside of the paper

4.2.2   Inks

The electrode layers were rotary screen printed using graphite and activated carbon inks. Graphite inks were applied onto the metallized papers in order to provide the corrosion shield for aluminium against the electrolyte and improve the electrical contact between aluminium and activated carbon layer. In the third printing trial, the sealing ink was also printed onto the electrode layers using rotary screen printing and flexography. The used inks were:

- Acheson Electrodag PF-407C graphite ink (first trial)

- Acheson Electrodag PF-407A graphite ink (from second to sixth trials)

- Activated carbon ink made of Norit Super 30 powder and chitosan binder (all trials)

- Paramelt Aquaseal X2234 sealing ink (third trial)

4.2.3   Print quality analysis

After printing, the print quality of the electrode layers was determined. The layer thickness was measured using Veeco Dektak 150 surface profilometer. The layer roughness and topography were determined using Veeco Wyko NT3300 white-light interferometer. The measurement area was 0.91 x 1.2 mm^2 (1st trial) and 297x226 µm^2 (2nd-6th trial). Both average roughness (R_a) and root mean square roughness (R_q) values were determined. The ink adhesion was determined using a simple tape test.

The visual quality of the layers was evaluated. The surface quality of the printed layers was also determined using NeoScope JCM-5000 JEOL scanning electron microscope (SEM) and Nanofocus µSurf Optical 3D topography measurement system. The sample size in the optical 3D topography measurement was 2.7 mm x 2.8 mm.

4.3   Results

4.3.1   First pilot trial for supercapacitor

The electrode layers, i.e. graphite and activated carbon ink layers were printed with rotary screen printing onto Stora Enso's Lunchbox 240 paperboard. The printing layouts are shown in Figure 4.2. The size of the graphite layers was 40 mm x 40 mm and activated carbon layers 20 mm x 20 mm. The activated carbon squares were printed in the middle of the graphite squares. The 10 mm wide graphite edges were reserved for the sealing of the supercapacitors.
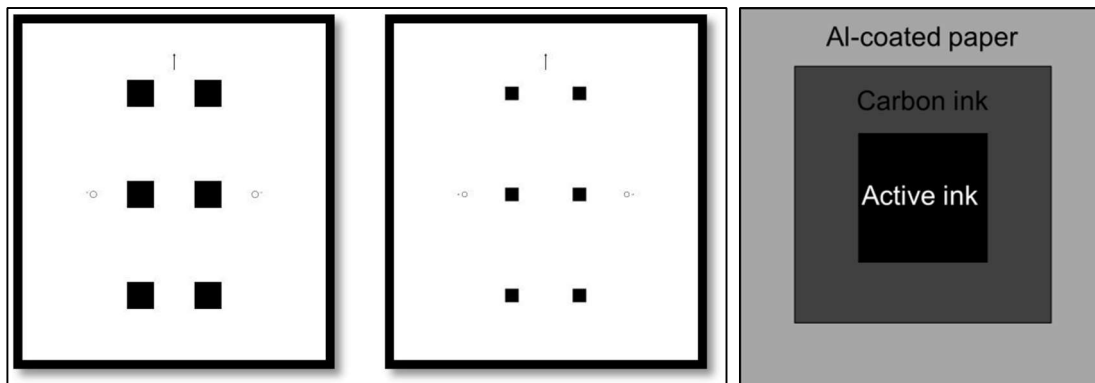

Figure 4.2. The printing layouts for the electrode layers. Graphite and activated carbon layer layouts are shown separately (left) and as printed onto the paper-based substrate (right).

Acheson PF-407C graphite ink was printed onto the aluminium coated paperboard. The printing speed was 2 m/min. The printed layers were dried using all the four hot air ovens of the printing press. The temperature of the ovens was 110°C since the paperboard warped and wrinkled at higher temperatures. The activated carbon layer was then printed onto the graphite layer at a speed of 2 m/min. The temperature of the ovens was decreased to 40-60°C. The first two ovens operated at 40°C and the last two ovens at 60°C. The activated carbon layers were smooth and no cracking occurred when bending the paperboard around the rolls. Photographs of the printing process are shown in Figure 4.3.
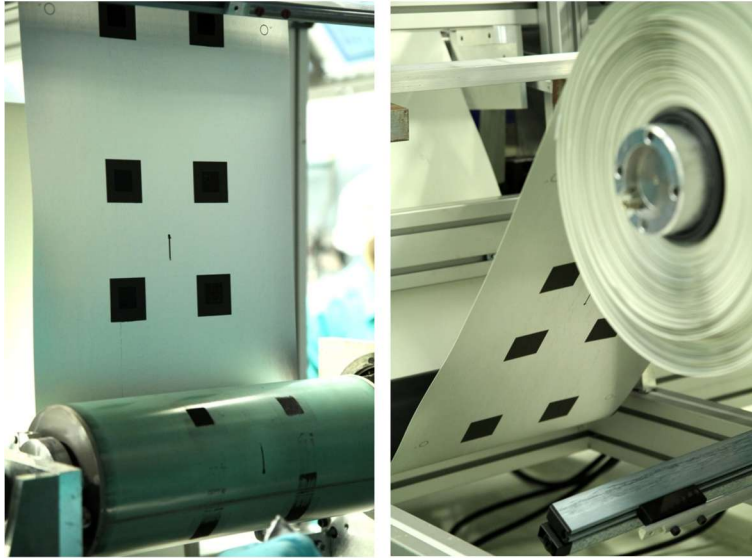
Figure 4.3. Photographs of the ROKO machine during the electrode printing.

The average thickness and roughness of the graphite and activated carbon layers are shown in Table 2.3. The thicknesses of these layers were similar to the typical values measured for hand-made supercapacitors. The activated carbon layer was significantly thicker and rougher than the graphite layer. Figure 4.4 shows the surface topography of the dried ink layers. The activated carbon layer had higher surface peaks and deeper surface valleys than the graphite layer.

It was noticed that the dried layers of activated carbon and graphite ink were quite rigid and brittle. When the electrodes were bent, the layers got relatively easily detached from the aluminium surface. Thus the adhesion between graphite and aluminium was rather poor. Possibly the heat treatment of graphite ink was not effective enough to cure the ink binder completely. The effect of the different drying times in laboratory oven on the ink adhesion was tested after the first trial. However, the ink adhesion did not improve even if the drying time was significantly increased. In addition, no significant differences in adhesion were seen between Acheson PF-407C and Acheson PF-407A inks.

Table 2.3. Thickness and roughness for supercapacitor layers. The measurement area of the roughness measurement was 0.91 x 1.2 mm^2 (5.2x).

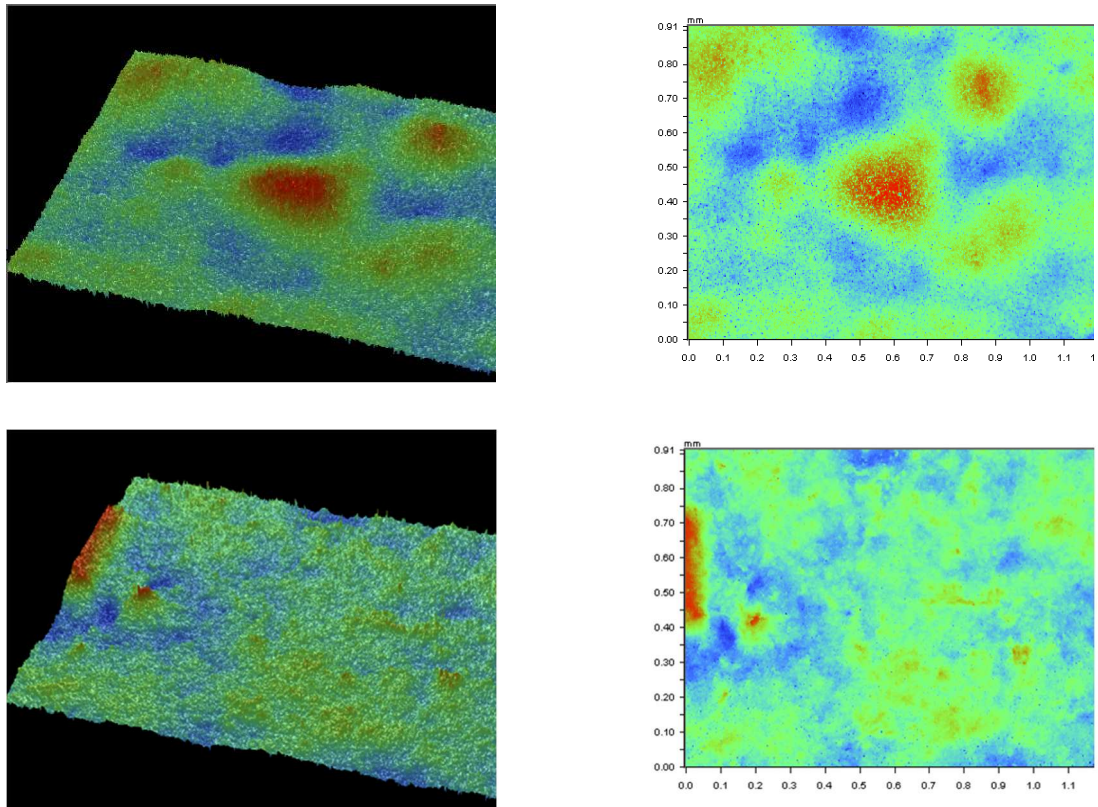| Layer	Thickness [μm]	R_a [μm]	R_q [μm]
Graphite	20	1.5	2.0
Activated carbon	92	3.7	4.9

Figure 4.4. Surface topography of graphite ink (bottom) and activated carbon ink (top) layers. Magnification was 5.2X (0.91 x 1.2 mm^2).

4.3.2   Second pilot trial for supercapacitor

The main goal of the second printing trial was to solve the ink adhesion problem. Walki C1S paper having a plastic layer between the base paper and the aluminium foil was used to achieve better ink adhesion and allow the use of higher drying temperatures. During the second trial, web curling in the drying section was severe and the web path had to be changed so that the wrap angles on the guiding rolls straightened the web. Only two of the four dryers were used at the drying temperature and one at room temperature with blasting.

The printing layout was similar to that used during the first trial run (Figure 4.2). Electrodag PF-407A ink was printed using rotary screen printing onto the C1S paper and dried using two hot air ovens at 120-140°C. Acheson PF-407A ink was chosen over Acheson PF-407C according to the recommendations of the supplier. After this, the activated carbon ink was rotary screen printed on top and dried in two ovens at 80-90°C. Both graphite and activated carbon inks were printed at a speed of 2 m/min.

The printability of both inks was good and thick layers were obtained. Graphite ink layer had good coverage but the activated carbon ink layer had pinholes resulting from the screen clogging due to too fast drying of the ink. Ink adhesion was clearly better than in the first trial due to the higher drying temperature and different substrate. Extra drying in a laboratory oven at 120°C after the rotary screen printing improved clearly the ink adhesion as one can clearly see from Figure The longer the drying time, the better the adhesion became.
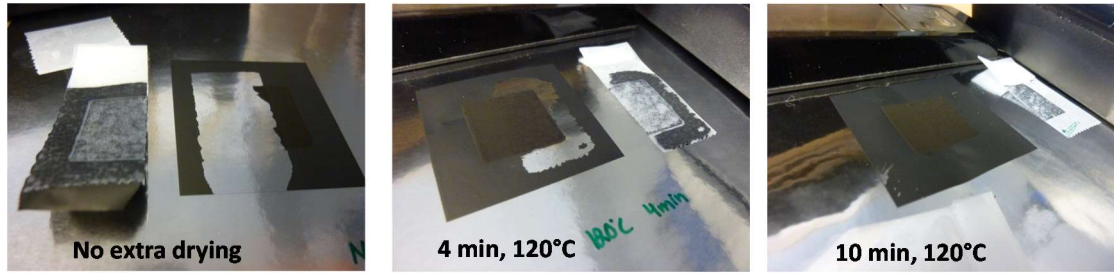
Figure 4.5. Influence of extra drying in laboratory oven on ink adhesion to aluminium layer of the paper.

Ink layer evenness was quite good although the coarse screen mesh patterns were visible. The maximum thickness difference was 20 μm. This is described in *Figure 4.6*Figure 4.6 where the surface of active ink layer is presented using optical 3D topography measurement.

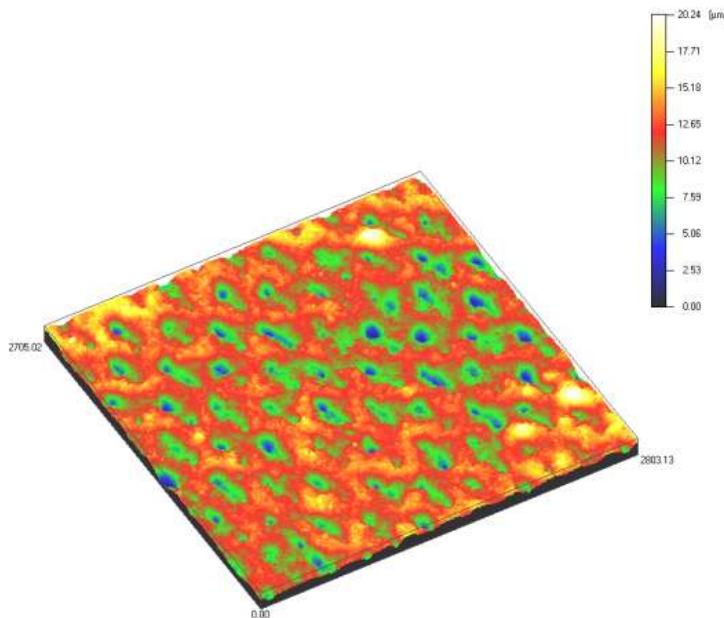*Figure 4.6. Optical 3D topography measurement of the printed active layer surface. Blue (thin) points reflect the used mesh count of 64 inch^{-1}.*

The graphite layer was 20-23 μm thick which was similar to the layer thickness obtained in the 1st print run. However, the activated carbon layer thickness was only 55 μm which was 40 % smaller than in the 1st trial run. This was mainly caused by the variations in the ink viscosity or solids content from trial to trial. The average layer roughness (R_a) of the graphite and activated carbon layers was 0.9 μm and 2.4 μm, respectively. These values were lower than in the previous trial (Table 2.3) resulting probably from the different substrate and more efficient drying that might level the layers more efficiently. After this trial run, it was decided to install new guiding rolls between every drying unit in order to decrease the paper curling and to enable the use of all the drying ovens at higher temperatures to achieve longer and more efficient drying.

4.3.3   Third pilot trial

In the third trial, the purpose was to determine the influence of the IR drying on the ink adhesion and print quality; improve the ink adhesion by introducing new guiding rolls that enable longer and more efficient drying; and apply Aquaseal material for sealing purposes using rotary screen printing and flexography. The printing layout had three times more capacitors per screen than the earlier version. Furthermore, Aquaseal layer framed the electrodes. The printing layouts are presented in Figures 4.7 and 4.8.
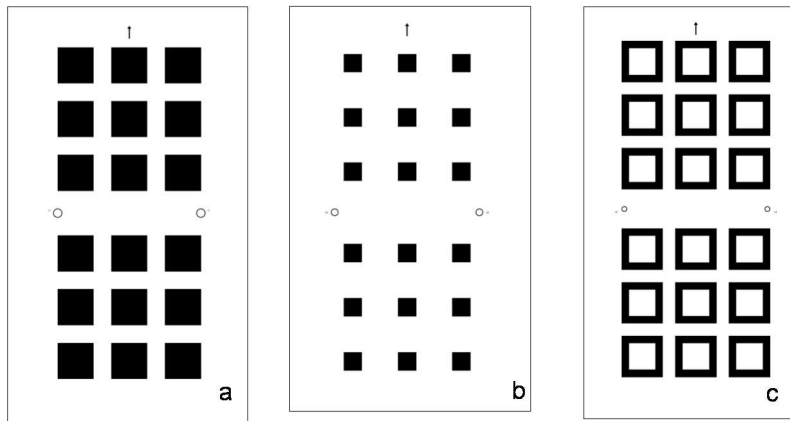

Figure 4.7. The printing layouts for third trial: a) graphite layer, b) activated carbon layer and c) Aquaseal layer.
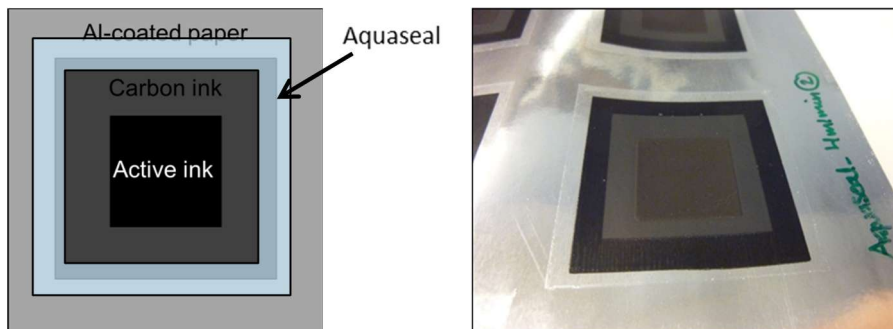

Figure 4.8. Printed supercapacitor with Aquaseal layer.

Graphite and activated carbon inks were printed onto Walki C2S paper and Stora Enso Lunchbox paperboard at a speed of 2 m/min. Walki C2S paper had polymer layers between the base paper and the aluminium foil and also on the back side of the paper which made it easy to handle in the printing machine. In the case of C2S paper, the graphite layer was dried either by using all the four ovens at 140°C or by replacing the first oven with the IR dryer (5 kW) and keeping the temperature of the next three ovens at 140°C. During the IR drying, the printing speed was decreased to 1.5 m/min. Activated carbon layer was then overprinted and dried in all the four ovens at 140°C. Finally, Aquaseal sealing material was printed with rotary screen printing and flexography and dried at 120°C in all the four ovens of the printer. The printing speed was 2-4 m/min. In the case of Lunchbox paperboard, the graphite ink and activated carbon inks were dried in all the four ovens of the printer at 95-110°C. The temperature had to be decreased because of the cross directional wrinkles in the aluminium surface. One reason for the wrinkles was the dimensional changes of the base paperboard under the aluminium.

The new extra guiding rolls worked well. The substrates went through the process without severe curling even though the drying temperature and capacity were much higher. Adhesion, roughness and surface topography are presented in Figures 4.9, 4.10 and 4.11. The graphite layer thickness was 20 µm and activated carbon layer thickness 88 µm. The

printability of both inks was good and rather good layer coverage was obtained. Some small holes were seen in the activated carbon layer because of the screen clogging caused by the fast ink drying. PF-407A ink layer was smoother than the active ink layer (Figure 4.10) mainly because of the differences in the layer thickness and ink rheology.IR drying increased the layer roughness slightly since the solvents were removed faster. The surface topography of the printed layers is presented in Figure 4.11. Adhesion improved significantly when PF-407A layer was printed onto C2S substrate and the layer was IR-dried or extra oven dried (Figure 4.9). On Lunchbox the adhesion was lower than on C2S and significant improvement was not found even after 15 min extra drying in oven.The main limitation of the Stora Enso Lunchbox seemed to be the temperature resistance.
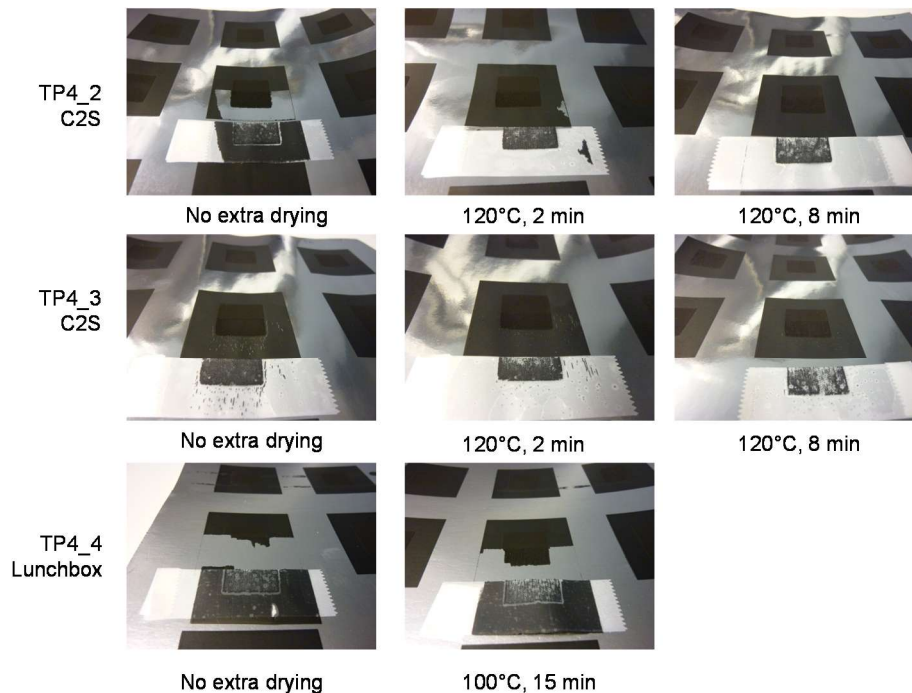

Figure 4.9. Influence of drying conditions on the ink adhesion based on tape test. TP4-2 is Walki C2S air drying T=130 ºC, 2 x 2min, TP4-3 is Walki C2S IR drying 5kW, 12 s + air drying T=130 ºC, 2 x 2min and TP4_4 SE Lunchbox air drying T~100 ºC, 2 x 2 min. Time and temperature of extra drying is described below photographs.
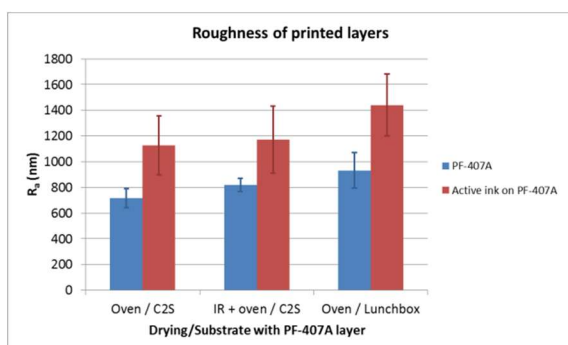

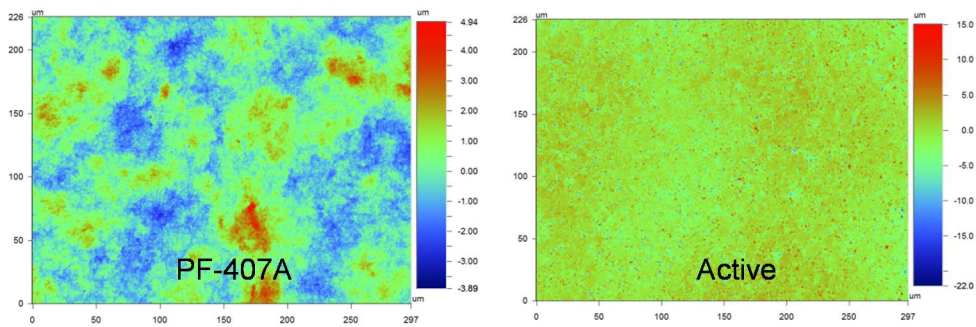*Figure 4.10. Roughness values of the printed layers.*

Figure 4.11. Surface topography of the printed layers based on Veeco Wyko NT3300 white-light interferometer measurements. Graphite ink and activated carbon ink layers were printed onto the C2S substrate.

Figure 4.12. Flexo printing unit during the application of Aquaseal layer. Flexo printing worked well with Aquaseal liquid since it was originally developed for flexography.

The application of Aquaseal dispersion for sealing purposes of capacitors was tested using both rotary screen and flexo printing methods. The viscosity of Aquaseal was too low for the rotary screen printing but the flexographic printing was successful (Figure 4.12). However, the layer thickness was only 0.5-0.6 µm because of the low ink transfer volume, low ink viscosity, and indirect ink transfer. The layer roughness was 280 nm on C2S paper and 900 nm on the graphite layer. The low thickness and high roughness on the printed layer indicated that the layer could not properly cover the printed layer edge, thus not being able to seal the supercapacitors properly.

4.3.4   Fourth trial

The goals of fourth trial were as follows:

- Larger area of the supercapacitor for achieving higher capacitance.

- Influence of the IR drying on the ink adhesion and on the print quality.

- Longer and more efficient pilot drying using additional IR drying in NICO and ROKO in order to achieve better ink adhesion.

- Increase the activated carbon layer thickness.

Graphite and activated carbon inks used in second and third trial were chosen also for the fourth trial. Both Walki C2S paper and Stora Enso Lunchbox paperboard were used. The printing layout is presented in Figure 4.13 as well as NICO printing machine which was used for the additional IR-drying of the printed samples.
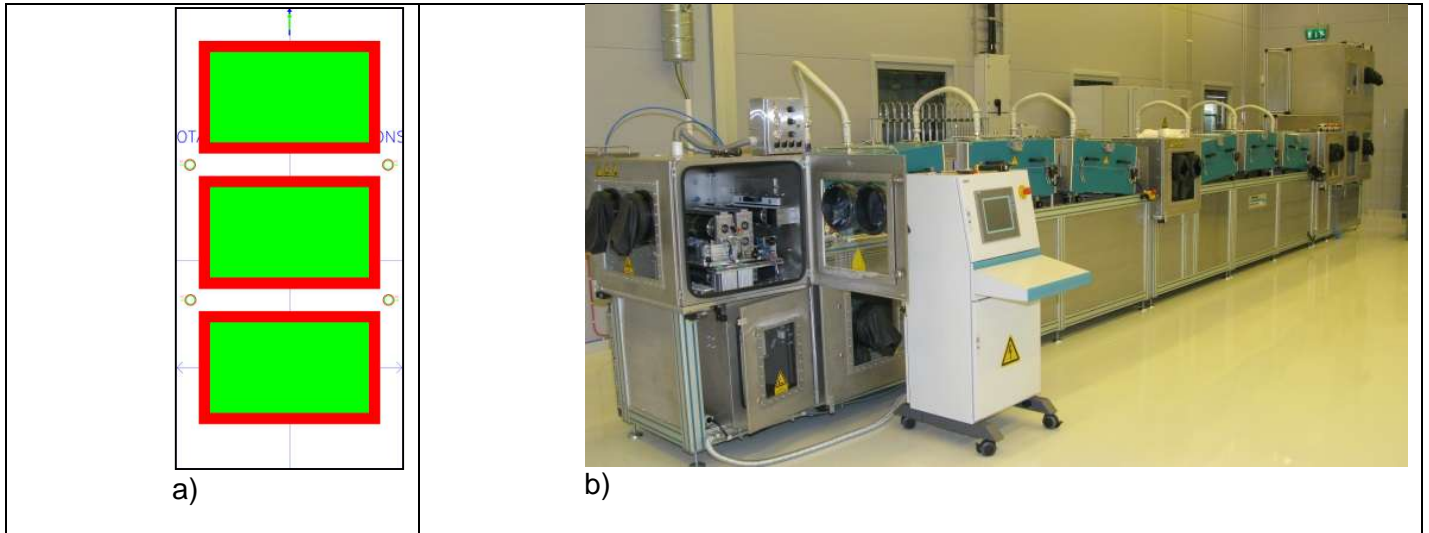

a)   b)

Figure 4.13. The fourth trial: a) layout, b) NICO printing machine used in additional IR drying.

Graphite and activated carbon inks were printed onto Walki C2S paper at the web speed of 2 m/min. The graphite ink layer on C2S paper was dried by using all the four ovens at 140°C. Activated carbon layer was then printed and dried using the four ovens at 140°C. Half of the samples were extra dried with ROKO and half with NICO. Additional drying with ROKO in the case of C2S paper was done at a speed of 1.5 m/min using both the IR drying unit (5 kW) and three hot air ovens at 140 ⁰C . Extra drying in NICO was done using 6 IR drying ovens at 100⁰C. The web speed was 2 m/min. In the case of Lunchbox paperboard, the graphite ink was printed at a speed of 1 m/min and dried at 95-110°C. The activated carbon layer, for its part, was printed at a speed 2 m/min and dried at 100-110°C. Half of the samples were extra dried with ROKO using both IR drying (2 kW) and hot air drying at 100°C. The speed was 1.5 m/min. The extra-drying with NICO was performed similarly as with C2S substrate.

Adhesion and surface topography are presented in Figures 4.14, 4.15 and 4.16. The printability of PF-407A was good, but active ink had clumps. Active ink layer was more uneven and brittle than in the earlier trials. The reason was probably old ink since the active ink was made a few weeks before the run. Graphite layer had good adhesion to C2S paper on the edges and poor otherwise directly after the printing (Figure 4.14). Printing and drying of the subsequent active ink layer improved the graphite layer adhesion and the extra IR-drying had only a slight effect. PF-407 ink had poor adhesion to Lunchbox paperboard, but extra IR drying with NICO improved its adhesion.

Microblistering was noticed on the printed samples (Figure 4.15). The reason was probably too high drying temperatures and generally too intensive drying. Some microblistering was also found in the earlier samples. Corrosion troubles in assembled capacitors were later found. Together these two observations forced to improve the print quality and eliminate the microblistering by decreasing the drying intensity and temperatures.

Graphite layer thickness was 18-21 µm and roughness 760-850 nm depending on the substrate. Smoother but thicker layer was obtained on C2S paper than on Lunchbox paperboard. BY and BZ-type screens were tested for active ink. Both had the same mesh size (64 lines/inch) but BZ screen transferred significantly more ink. The layer thickness was 80-84 µm with BY screen and 170 µm with BZ screen. The screen type had no significant effect on the active ink layer roughness (1.1-1.4 µm) but BZ screen made the layer

unevenness worse. BZ screen produced a more brittle layer which cracked more easily than the layer made using BY. This was caused by the very high layer thickness.
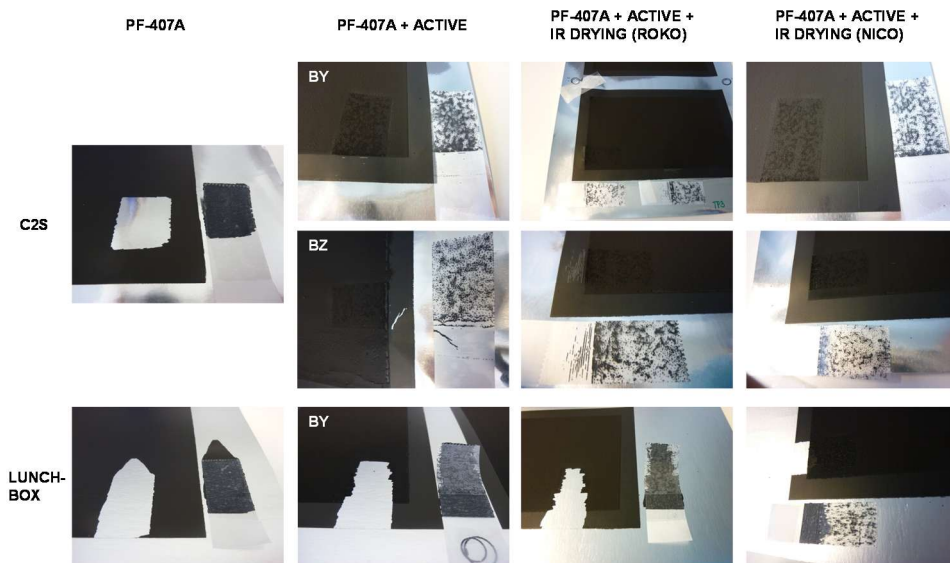

Figure 4.14. Influence of drying conditions on the ink adhesion based on tape test.

Figure 4.15. Light microscope photo about microblistering on the surface of printed Walki C2S. Too intensive drying created the microblistering. Evaporable moisture broke the surface of thick graphite ink layer and produced even pinholes. This observation forced to decrease the drying temperatures.
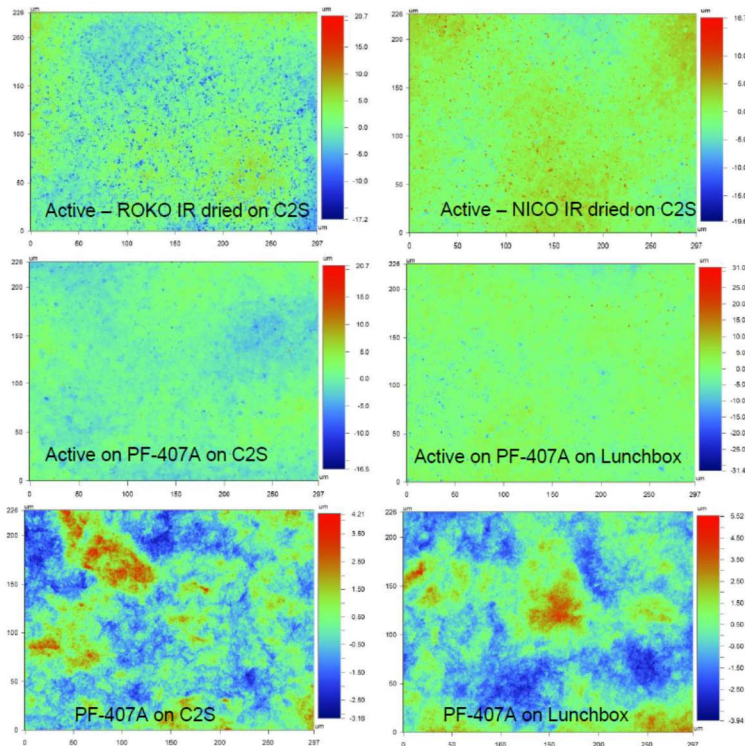
Figure 4.16. Surface topography of the printed layers on different substrates. Additional IR drying increased the layer roughness.

4.3.5   Fifth trial

The main purpose of the fifth trial was to eliminate the microblistering by decreasing the drying temperatures and by improving the ink handling. In addition, the graphite layer thickness was decreased and layer evenness improved by using finer screen and slightly thinned ink. Only Walki C2S paper was used in the fifth trial. The layout was similar to earlier in the fourth trial. Graphite layer was printed at a speed of 1 m/min using BY (64 1/inch) and 215V (215 1/inch) screens. In addition, thinned ink (more PGMEA solvent added) was printed using 215V screen. The activated carbon ink was then overprinted at a speed of 1 m/min and using BY screen. The printed electrodes were then extra dried using all the four ovens of the printer. Drying unit temperatures were 90ºC, 90ºC 100ºC and 120ºC in every printing round (graphite ink printing, active ink printing and extra drying).

The printability of the graphite ink was good. The finer 215V screen type gave better edge definition and lower thickness (Table 4.4) but the layer roughness was approximately the same as in the case of coarser BY screen. However, SEM inspection revealed that BY screen gave higher macro-roughness and unevenness than 215V screen. This is illustrated in Figure 4.17. Thinner graphite ink had only minor effects on the layer quality. Adhesion was good although the drying temperatures were lower than earlier. On the other hand, drying times were prolonged by decreasing the printing speed to 1 m/min so that ink had enough time to settle and interact with the paper. Microblistering was not found any more in printed samples, as seen in Figure 4.17 mainly since ink solvents were removed slowly enough during drying. Despite the eliminated microblistering, corrosion spots in assembled capacitors were later found in all cases. Activated carbon layer was slightly thinner than previously since higher squeegee pressure was used during printing. However, the layer was thicker than the graphite layer and cracked easily.

Table 4.4. Thickness and roughness values of ink layers with different screens in fifth trial.

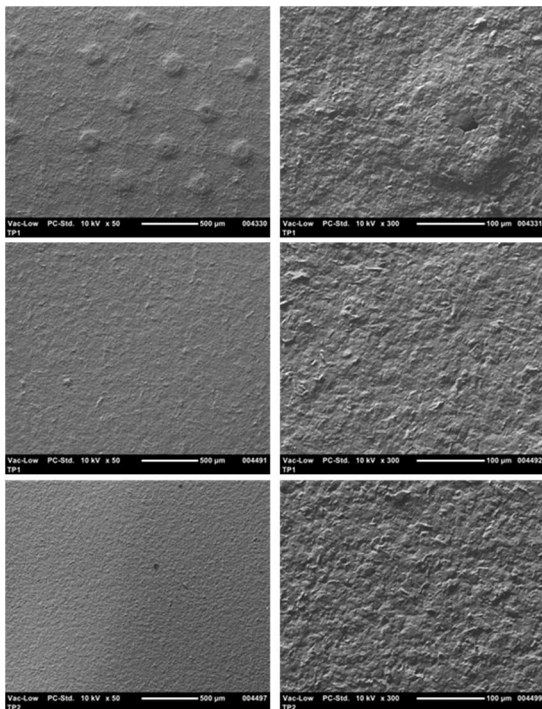| Screen type	Thickness [μm]	Roughness [nm]
Graphite layer		
215 V (215L/inch)	7 ± 1	800 ± 30
BY (64L/inch)	18 ± 2	770 ± 40
Active layer		
BY (64L/inch)	76 ± 7	1630 ± 570

Figure 4.17. SEM images of the printed graphite layers. Microblistering is clearly visible in the samples printed in the fourth trial run (top) but it disappears in the fifth trial (centre, bottom). The effect of the screen type is also shown in the case of BY (centre) and 215V (bottom) screens. The magnifications are x50 (left) and x300 (right).

4.3.6   Sixth trial

The purpose of the last printing trial was to eliminate any holes in the graphite layer so that the electrolyte cannot get into contact with the aluminium surface of the paper. This was done by printing two graphite layers using finer screen. Another goal was to improve the printability and flexibility of the activated carbon ink.

Two graphite ink layers were printed using 215V screen onto C2S paper. These two layers were deposited and dried in separate print runs The printing speed was 1 m/min and the temperatures of the ovens were 90°C, 90°C,100°C, and 100°C. The intention was that if there would be a pinhole in one layer the other layer would cover this defect. Both the earlier active ink and the new more flexible active ink were used. The new ink was based on 3 wt % addition of glycerol to active ink. The printing speed was 1 m/min and the temperatures of the ovens were 90°C, 90°C,100°C, and 100°C. The layout is presented in Figure 4.18. The size of the electrode was the same as on the fourth and fifth trials but the second graphite layer was slightly smaller for easier registering.
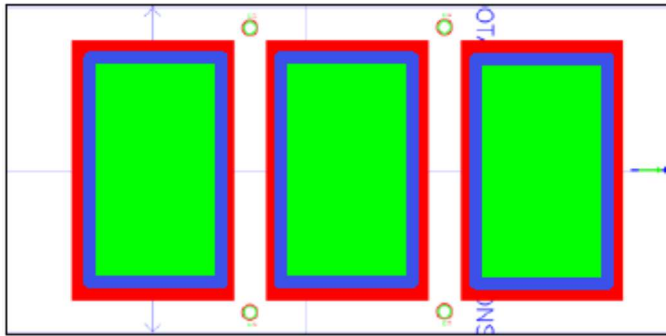
Figure 4.18. Layout of the sixth trial. Red and blue layers are the two graphite ink layers and the green layer is the active ink layer.

The graphite ink printability was good and the printed layer had sharp edges and good coverage without holes. The thickness and roughness of the printed layers are presented in Table 4.5. Double graphite layer thickness was only 10 µm and the layer roughness was at the same level as in the previous runs. This thickness was roughly 50 % smaller than when using the coarser BY screen. Activated carbon ink layers were approximately 60 µm thick and both inks were nicely printable. Glycerol containing active ink had better viscosity than the normal active ink but it created more pinholes. Generally printed layers had good adhesion, as seen in Figure 4.19.These printed electrodes were used for the demonstration purposes. Corrosion problems still existed even though print quality improvements were made.

Table 4.5. Thickness and average roughness values of the sixth trial.

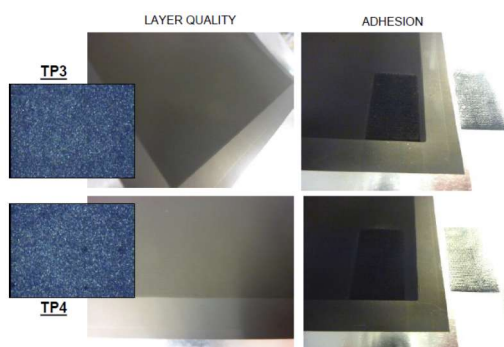| Layer	Thickness [µm]	Average roughness [nm]
Graphite (double layer)	10 ± 1	790 ± 30
Active (normal)	61 ± 8	1180 ± 230
Active (glycerol included)	63 ± 5	1560 ± 290

Figure 4.19. Layer quality and adhesion of the 6th trial run. TP3 is the normal active ink and TP4 its glycerol version. Microblistering bubbles were not found and print quality was relatively even.

4.3.7 Morphological characterization of printed electrodes

The morphology of the VTT-printed electrodes was characterized utilizing both confocal white-light microscopy (COM) and scanning electron microscopy (SEM) techniques. From all

printed batches of electrodes, COM-images of the active carbon (AC) layer have been provided to the manufacturing party (VTT Oulu). Surface roughness analyses have been performed for the samples, investigating the effects of the different drying conditions on the morphology of the AC layer. AC print layer thicknesses have also been studied, and found to be in good agreement with those reported by VTT, Oulu.

The printing quality and coverage of the protective graphite layer has also been investigated utilizing COM-imaging, in order to remedy the aluminium corrosion issue. The so-called microblistering effect of the graphite layer has been studied, and found to be one of the sources for the pinholes in the protective graphite layer. A microblister with a corresponding pinhole is shown in Figure 4.20, where the profile (red line) is drawn through the microblister and pinhole.
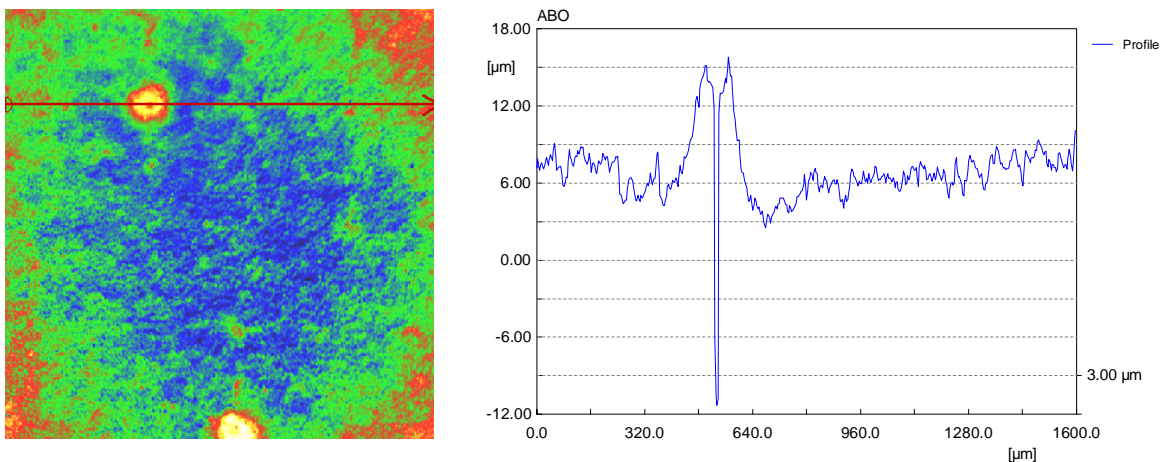
Figure 4.20. Microblister and pinhole in graphite layer. Profile taken along red marked line.

Plane and cross section imaging with SEM for some of the samples were also performed, especially with the focus of investigating the effect of cracking of the AC layer, as the hypothesis was that cracks in the AC layer might propagate through the graphite layer down to the aluminium substrate, which could act as points of initial corrosion attack. A SEM image of such a crack is shown in Figure 4.21.
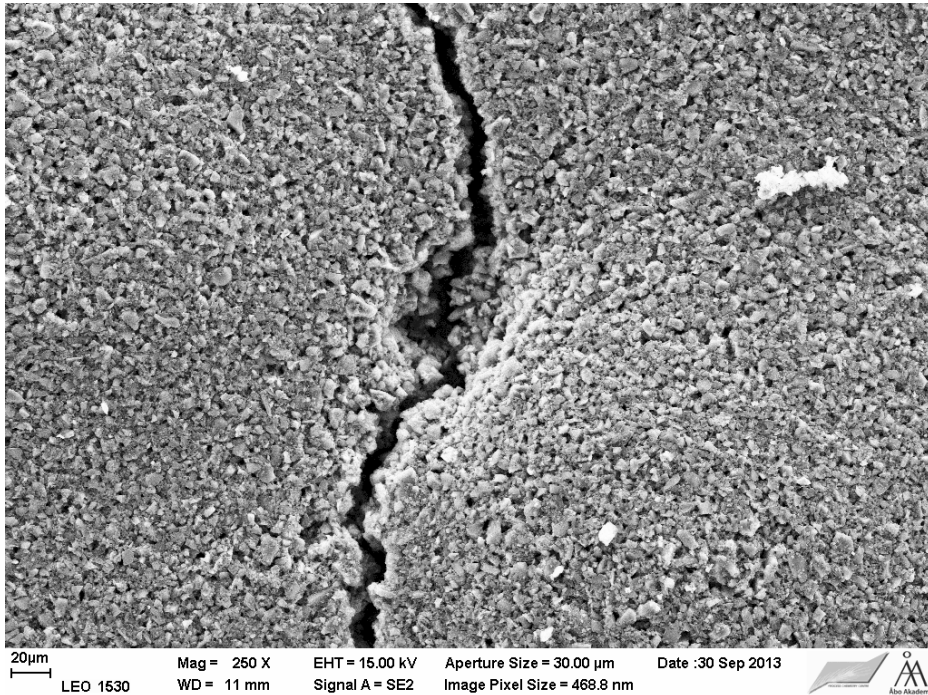
Figure 4.21. SEM image of crack in activated carbon layer.

4.4   Pilot scale printing: conclusions and suggestions

Pilot scale printing showed the feasibility of the printing of supercapacitor electrodes. Further work is needed developing the materials and optimizing the process parameters. The printing properties of inks including long drying time requirements are not yet completely ready for the needs of flexible fabrication of supercapacitors.

Some recommendations for future work:

- Active ink properties have to be developed so that active ink layer is less brittle.

- Screen material is sensitive for acidic inks. Screen materials have to be developed more suitable for acidic inks or ink material should be less acidic.

- Two layer graphite ink option can be used if this is needed for avoiding corrosion troubles.

- Long drying time is a challenge. Drying times even longer than 10 min may be difficult in effective production. On the other hand too intensive drying leads to microblistering of thick ink layers.

4.5   Printing of ionic liquid doped electrodes

In order to investigate the positive effect of Reline on Chitosan (see section above for the theory), and if it could be used to "un-screen" the surface of the AC from the Chitosan, we investigated to print AC electrodes with and without Reline in the printing ink (6,5% IL).

Screen prints with IL in ink

Figure 4.13. Semi-automatic screen printer and IL containing ink + print with AC and Reline.

The tests were conducted by using the VTT recipe (used in Roko printing trials) for the AC print – and to this add 6,5% Reline (same amount as the Chitosan). Printing was done using in house semi-automatic screen printer and printing the two different formulations after each other. Summary of the results are shown in figure 4.14 and the prints analysed in confocal microscope can be seen in figure 4.15.

Comparison – with or without IL

	E_{eff}	C_{STEADY}	L1 30min	L2 30min	L2 60min
Standard electrodes*	0.98	157mF	19µA	15µA	13µA
ÅA printed w/ Rel**	0.94	116mF	15µA	11µA	8µA
ÅA printed w/o Rel**	0.93	129mF	14µA	8µA	5µA

*Charged at 1mA
**Charged at 0.5mA
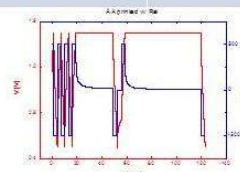Device: A=0.8 cm², d=1.3mm, BMIM-TFSI, in air

Figure 4.14. In house (FunMat) ÅA printed AC devices, compared to VTTs standard electrode devices.

From figure 4.14 it can be seen that the values of capacitances are all within the error margins, and no positive effect of using Reline within the printing ink can be detected. The in-house printed show a little lower performance compared to the VTT printed ones and this can be attributed to the difference in equipment used and also by the problems with ink-clogging of the screens, seen in the in-house experiments (see figure 4.15).
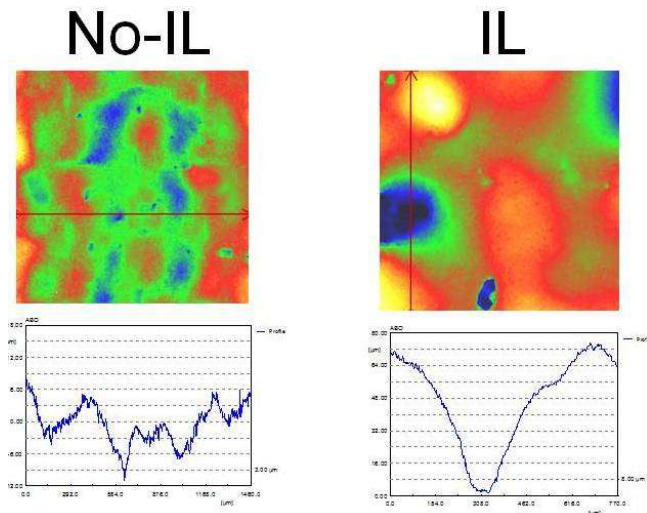
Figure 4.15. Confocal microscope images of the in-house prints, with-IL (IL) and without-IL (No-IL) printed electrodes.

In figure 4.15 one can see that the with-IL printed showed much more defects in the prints attributed to ink-clogging the screen (visually seen during printing). The with-IL ink was printed after the without-IL and the problem seemed to be a time issue (i.e. all prints got worse as the printing continued) and not an effect of the added IL. These results needs to be verified and also the IL content needs to be optimized (15, 30% in tests) to fully evaluate the effect of added Reline within the printing ink. This work is ongoing and a courser screen with mesh 54 compared to mesh 72 used here, will be ordered to diminish the effect of screen clogging.

5. WP4 Supercapacitor manufacturing

5.1   Supercapacitor structure

A schematic structure of a printed supercapacitor is shown in figure 5.1. The horizontal and vertical dimensions are not in the same scale. Typically the total thickness of the capacitor was 0.6-0.8 mm. Supercapacitors of two different size ranges were manufactured: the width and length of the smaller size were approximately 50 and 70 mm and for the larger size 100 and 150 mm, respectively. The geometrical electrode area of the smaller supercapacitors was 3-4 cm^2 and of the larger 84-112 cm^2.
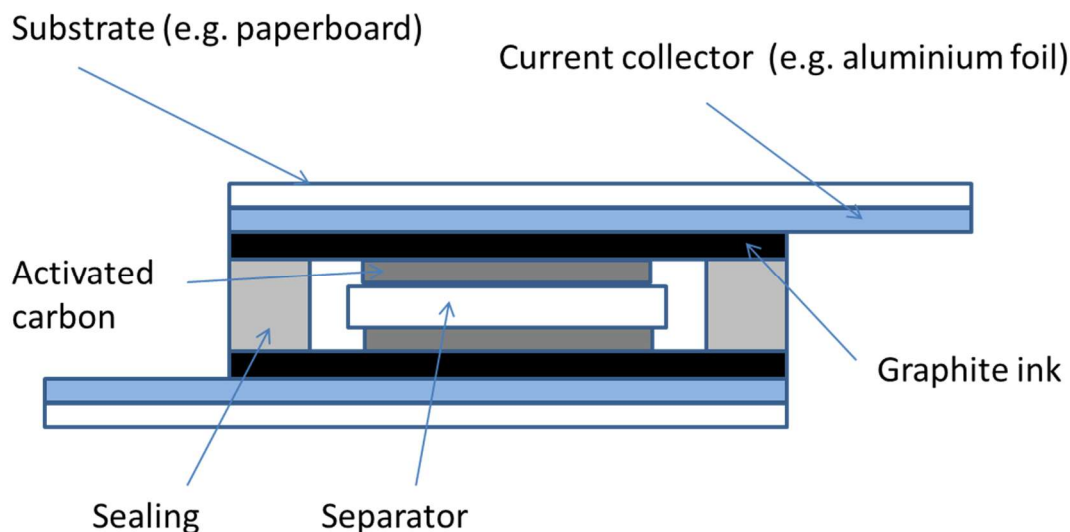

Figure 5.1. Schematic structure of a printed supercapacitor.

The graphite ink layer between metal current collector and activated carbon ink decreases the contact resistance and especially in case of aqueous electrolytes also protects the metal from corrosion. During the project in most cases Acheson PF407A graphite ink was used instead of the earlier PF407C grade. The main reason for the change was the faster drying obtained with the new grade. According to the manufacturer the cured layers are similar in both cases.

When assembling the supercapacitor the printed supercapacitor electrodes were positioned so that activated carbon layers were face-to-face. A frame made of PE or PET was put around the active layer and the separator to prevent contact the active layers. As adhesive hot melt foil or heat seal dispersion Paramelt Aquaseal was used. The electrolyte was applied on the electrodes and separator before heat sealing or after sealing three edges.

In all components one-fold cellulose separators were used. The basic alternative was NKK TF40 paper of 50 μm thickness. Also Dream Weaver separator was tested.
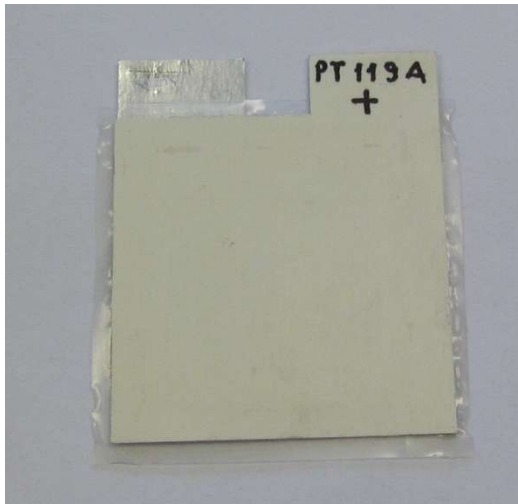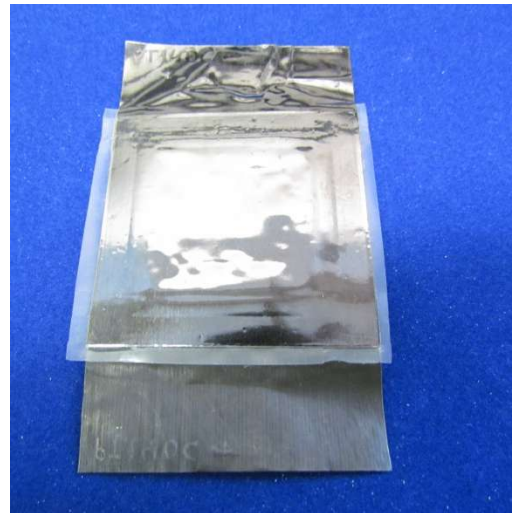
Figure 5.2 shows photographs of various assembled supercapacitors.
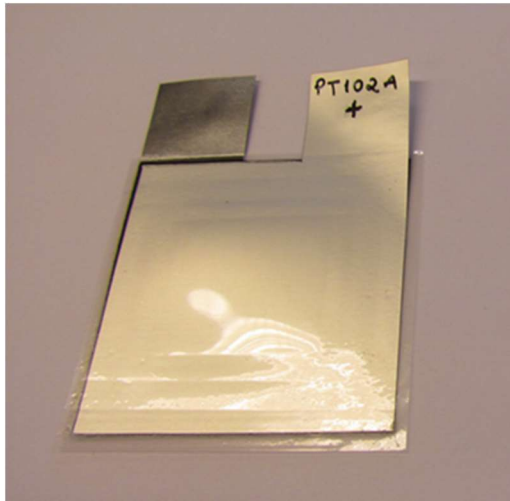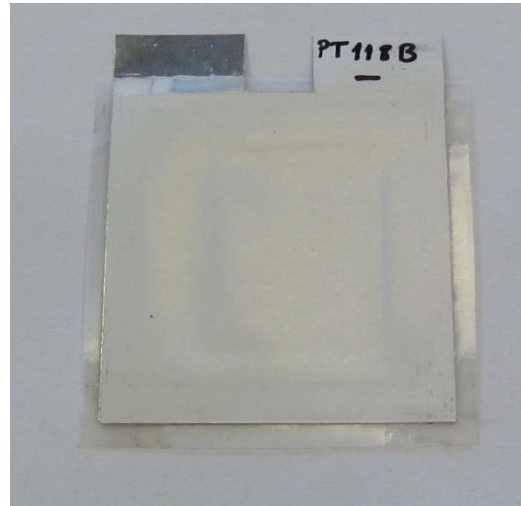
Figure 5.2. Supercapacitors (about 50 x 70 mm) made on Al/PET-substrate (a), Walki Al/paper C2S (b), Stora Enso Lunchbox Al/cardboard (c) and titanium coated aluminium foil (d). Supercapacitor (about 100 x 150 mm) made on Al/PET-substrate (e) and titanium coated aluminium foil (f).

5.2   Electrical properties

5.2.1   Measurement procedure

The electrical properties of the supercapacitors were measured using Arbin Supercapacitor Test Station. Charge-discharge curves were measured at constant current of 1 - 50 mA for small size range supercapacitors between 0.2 and 1.2 V for components with aqueous electrolyte and also between 0.4 and 2.5 V for components with organic electrolyte. For larger components current up to 1 A was used. The measurement procedure included first three charge/discharge cycles of which the third cycle was used to define the efficiency of the supercapacitor. After this the voltage was kept at the maximum voltage for 30 minutes and the capacitance was defined from the average slope between 80 % and 40 % of the maximum voltage during discharge with constant current. The voltage was again increased to maximum level and the current was monitored. The leakage current was defined to be the current needed to maintain the potential after 1 hour. The capacitance and leakage current definition were thus made as guided in the IEC 62391 standard. Figure 5.3 shows a typical measurement procedure. The equivalent series resistance values were also defined with the Arbin SCTS equipment using a built-in internal resistance measurement procedure as well as IR-drop method in the beginning of the discharge step.
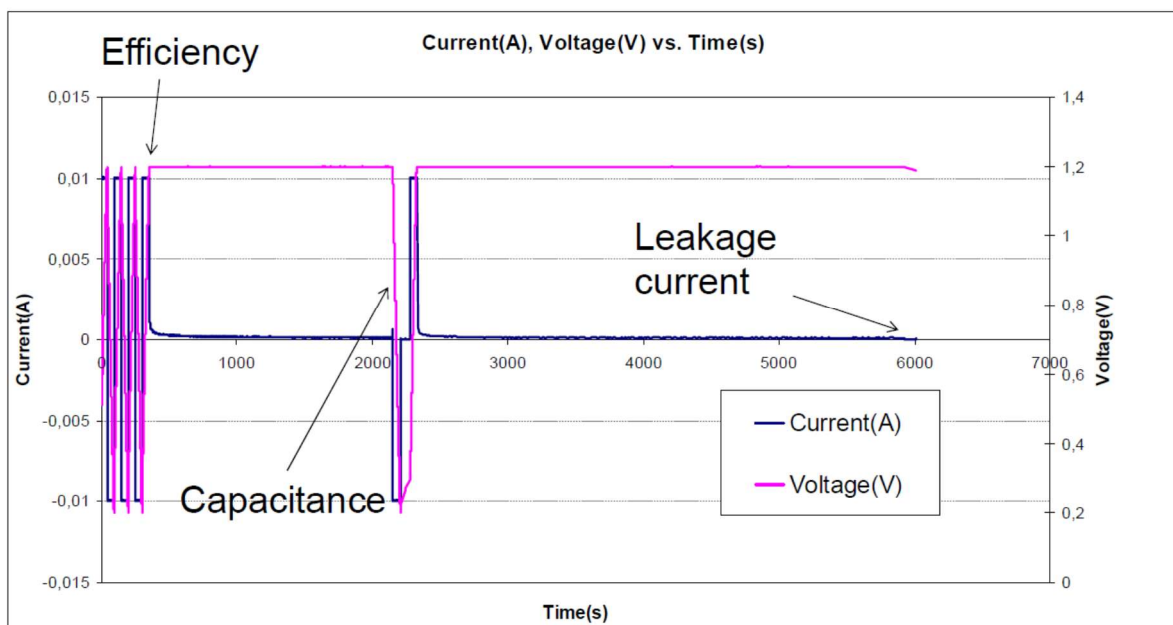
Figure 5.3. A typical measurement cycle.

5.2.2   Capacitance and voltage

The capacitance values of the majority of the smaller range supercapacitors were of the order of 0.1 – 0.6 F. The variations were due to changes in electrode material, electrolyte and in the geometrical area of the activated carbon layer. Typically water based electrolyte resulted to higher capacitance value than organic electrolyte. Depending on the electrolyte and thickness of the electrode the larger 100 x 150 mm supercapacitors had 5-20 F capacitance.

The specific capacitance measured for Norit Super 30 activated carbon electrodes was 19 – 25 F/g when defined for 2-electrode system. For 1-electrode system this would translate to 76-100 F/g. In these figures the electrode mass includes also the chitosan binder. The specific capacitance of the activated carbon electrode supercapacitors with acetonitrile or propylene carbonate electrolyte has been also about 20 F/g.

According to literature information MnO_2 should have higher specific capacitance than activated carbon. This was the case also in some of our MnO_2 supercapacitors since at best about 30 % smaller mass of MnO_2 gave the same specific capacitance as activated carbon.

The maximum voltage of a supercapacitor is basically determined by the electrolyte. With aqueous electrolyte the practical maximum voltage is about 1.2 V since the theoretical dissociation voltage of water is 1.23 V. By using organic electrolyte such as propylene carbonate it is possible to charge the supercapacitor to about 2.7 V.

The use of asymmetric structure consisting of activated carbon and MnO_2 electrode had been reported to facilitate voltages up to about 2 V with aqueous electrolyte. This is explained by surface reactions on MnO_2. According to our results continuous high voltage level (e.g. 1.8 V) for several days causes water electrolyte dissociation. Thus the high voltage compared with conventional aqueous supercapacitors can be used only when the component is continuously cycled as explained in chapter 2.1.3.

5.2.3   Equivalent series resistance

The equivalent series resistance (ESR) values for smaller size aluminium foil current collectors with aqueous electrolyte were typically 0.4 – 1 Ω for supercapacitors with 3-4 cm^2 geometrical active area. The ESR decreased to about 0.03-0.05 Ω as expected when scaled to larger 100 x 150 mm supercapacitors. With propylene carbonate electrolyte the ESR values increased by about 30 % and with EcoEng 212 (EMIM-ESU) RTIL the ESR was about 10 times higher than with aqueous electrolyte.

The ESR values measured for activated carbon supercapacitors having different sodium salts (NaCl, $NaNO_3$, Na_2SO_4) did not show considerably differences, possibly the sulphate alternative had slightly higher ESR. The use of aqueous choline chloride electrolyte increased the resistance to 2-5 Ω, but it should be taken into account that the choline chloride urea concentration was only about 2.5 %.

No clear difference in ESR was obtained between DreamWeaver and NKK separators. The difference between papers of similar thickness was not expected to be big.

The ESR of the components having MnO_2 electrode was at its lowest below 1 Ω, but varied a lot depending on the MnO_2 structure, being 19 Ω at its highest.

5.2.4   Energy efficiency

The efficiency values are mainly dependent on ESR and self-discharge rate. With high charge/discharge current the effect of ESR on the efficiency is clear. For most smaller components the values were defined with 10 mA and 50 mA charge and discharge current and for the larger components with 0.2 A and 1 A current. In the case of 10 mA current the efficiency values for aqueous supercapacitors were 90-97 % and in the case of propylene carbonate electrolyte 80 – 93 %. For the larger components the efficiency with 0.2 A and 1 A

current was 95 and 87 %, respectively for aqueous electrolyte and 92 % with 0.2 A in the case of propylene carbonate electrolyte.

Since the efficiency is decreased by increased ESR, it is obvious that with organic electrolyte the values are not this good. In the case of smaller components for propylene carbonate the best obtained efficiency with 10 mA current was 92 % whereas 93 % was reached for the larger components with PC electrolyte when measured with 200 mA current.

5.2.5   Leakage current

There is a clear correlation between the capacitance and leakage current: the larger the capacitance is, the higher the leakage current becomes if the structure of the supercapacitor does not change in other ways. In earlier projects it had been found that in the case of water based electrolyte diluted oxygen increases the leakage. Because of this it is necessary to use oxygen-free electrolyte and take care of the oxygen barrier properties of the supercapacitor encapsulation. Typical leakage current value after 1 hour at 1.2 V for 0.5 F supercapacitors was about 10 µA.

The leakage current of the supercapacitors with organic electrolyte was measured both at 1.2 V, 2.0 V and 2.5 V. Typical leakage current values for these voltages in case of about 0.5 F supercapacitor were 2, 10 and 30 µA, respectively.

5.2.6   Life time

Supercapacitor life time can be discussed from two different points of view. When the supercapacitor is not used, its lifetime can be determined by electrolyte evaporation or corrosion phenomena. This can be called shelf-life that is defined in time units. Another way is to cycle the supercapacitor and define its electrical properties after different numbers of cycles.

In our earlier project the shelf-life of supercapacitors was originally mainly dependent on electrolyte evaporation rate. When water is evaporated, salt starts to crystallize which gradually decreases capacitance and efficiency. Without metal barrier layers preventing the evaporation of water the life-time was of the order of few months. By adding aluminium foil to act as current collector and simultaneously as barrier layer, the evaporation rate was decreased and after this the evaporation has not been an issue. The shelf-life exceeds 10 years from this point of view.

Supercapacitors with NaCl, $NaNO_3$ and Na_2SO_4 electrolytes were cycle tested between 0.1 and 1.2 V for up to 40000 - 60000 cycles. The electrical properties of the supercapacitors were defined periodically during the testing. The capacitance and efficiency as functions of number of cycles are shown in figures 5.4 and 5.5. The best results were obtained for $NaNO_3$ electrolyte. The result for Na_2SO_4 seems to the poorest. However, the position of the component had clear influence on the performance in its case, after 14000 cycles the component was turned. Thus the main reason for the behaviour before it can be due to gas bubble inside the electrolyte which prevented the full use of electrode surface area.
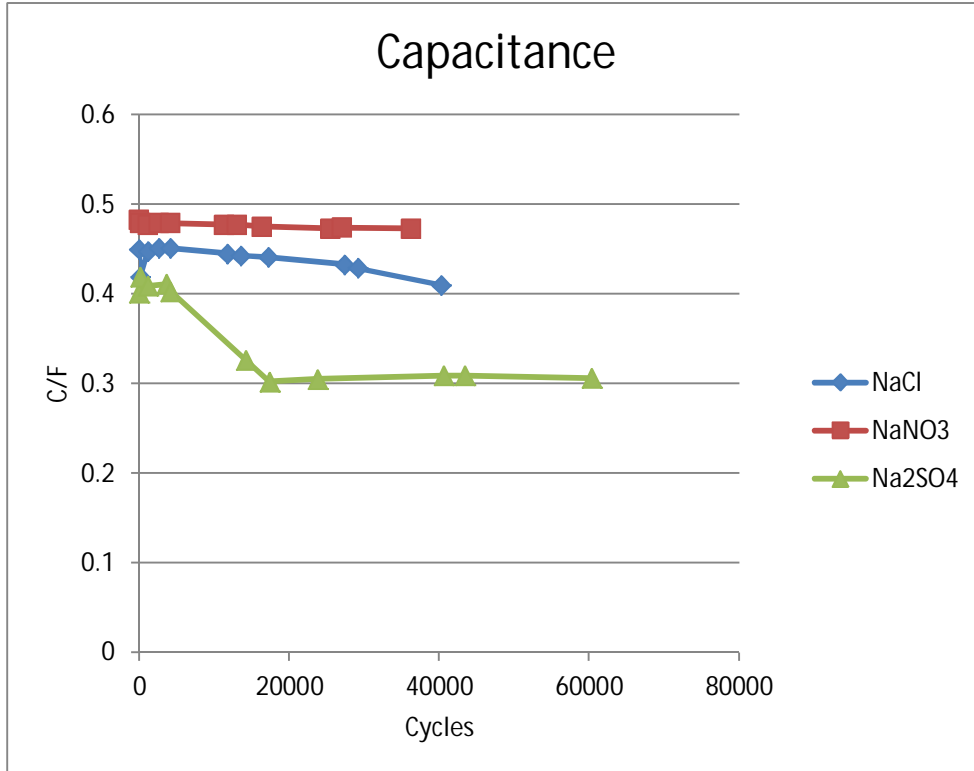
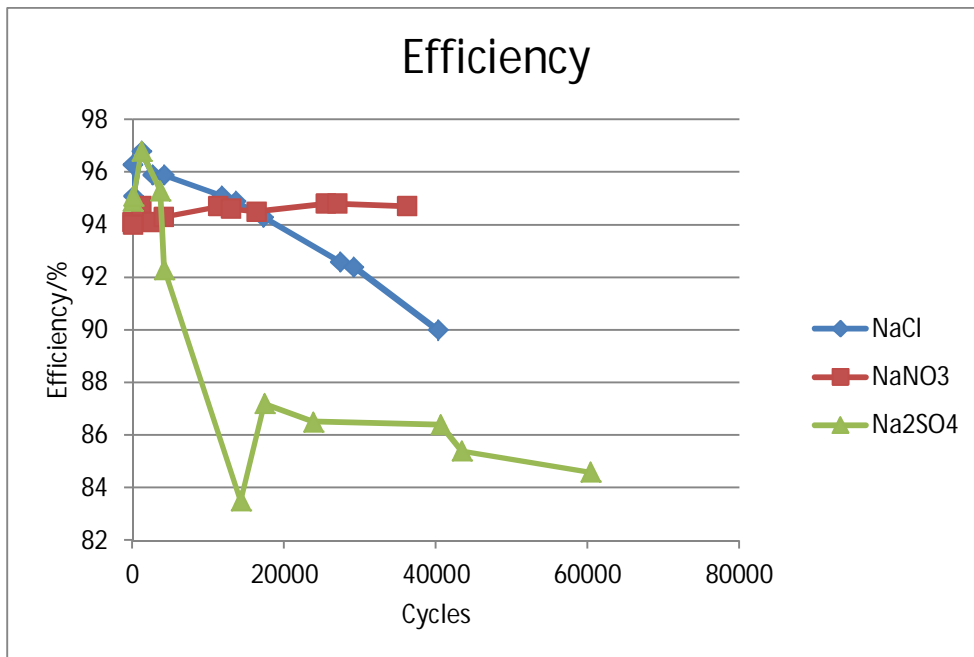*Figure 5.4. Capacitance change with various electrolytes after cycling.*

Figure 5.5. Change of efficiency with various electrolytes after cycling

Supercapacitors with PC electrolyte were cycle tested up to 2.7 V to compare if the higher voltage decreases the life-time. According to these tests the electrical properties do not remarkably deteriorate during the first 100 000 cycles indicating cycle life far beyond this.

5.3   Life cycle analysis and materials safety study

Life cycle analysis (LCA) was conducted from a manufacturing, use and disposability point of view. Materials choices, materials use and energy consumption were studied and reported where viable data was available. The LCA was divided into two main parts, the manufacturing and the disposal of the product. The manufacturing considerations are illustrated in Figure 5.6, where the blue coloured boxes indicate factors that are strongly specific to certain printing equipment and methods, and hence are difficult to assess properly in this study. The utilized RoKo printing facility, based at VTT Oulu, is a pilot printing facility, which is not optimized for energy and material efficiency, but rather for its flexibility and ease to modify according to present needs.
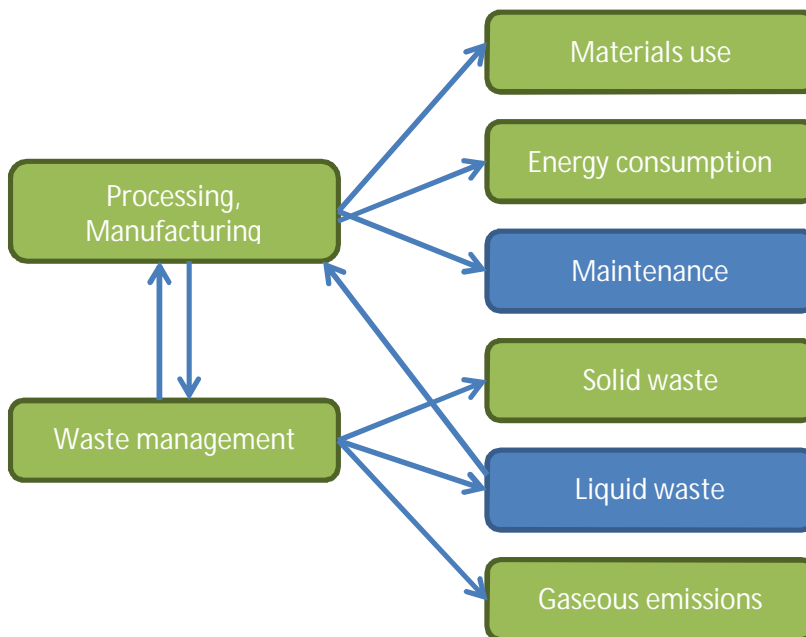

Figure 5.6. Manufacturing considerations for the LCA.

For the manufacturing part, the materials/chemicals associated in the manufacturing of the supercapacitor were identified and their respective impacts on the total material streams were assessed. This includes e.g. the material losses in the printing process, i.e. the efficiency of the printing substrate and ink usages. The chemical safety data (toxicity, handling, environmental impact, etc.) was extracted from the official materials safety data sheets (MSDS) for each chemical, provided by the supplier/manufacturer. An estimate of the energy demand of the manufacturing per supercapacitor was also made. The data for the energy efficiency and material streams are presently limited to the RoKo print facility, and the efficiency effect of e.g. up-scaling the printing process can only be an estimate. More specific LCA considerations at product level would require definitions of the geometry, capacity and voltage demand of the supercapacitor, as well as data for ink and substrate yields from the actual production printing facility.
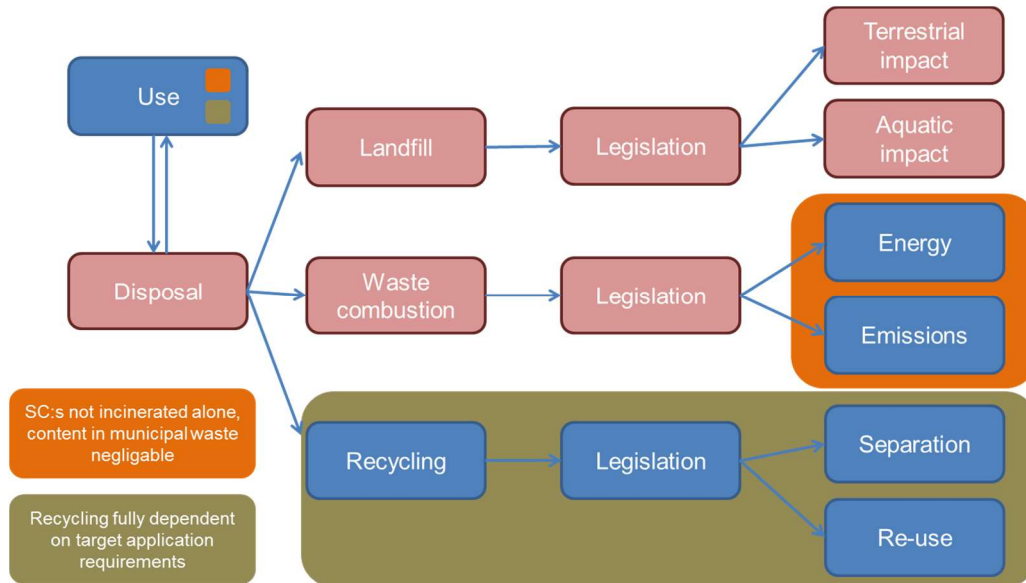
Figure 5.7. Use and disposal considerations for the LCA.

For the product use and disposal case, Figure 5.7, the relevant legislation was processed. For the disposability legislation both the landfill and the incineration case were assessed. Only a few potentially problematic compounds in the supercapacitor construct were found. Due to their extremely low amounts/unit and additionally their slow leaching rate due to the association with the print, the disposal of the product in landfill is considered to be safe. In addition, combustion was found to be safe.

The disposal case is also strongly dependent on the actual end product, where the supercapacitor is integrated, as the supercapacitor is not meant to be a stand-alone component. The present consensus is that the supercapacitor does not impose any further limitations on disposability and is only limited by the regulations regarding the end product itself.

6. WP5 Demonstrations

6.1   Materials for demonstrator prototypes

Successful development of a realistic RFID tag demonstrator necessitated that any additional tag electronics could be assembled onto a flexible laminate. For this purpose, etchable laminate for manufacturing thin, flexible printed circuit boards (PCBs) was found to be available in small quantities. The laminate has a 35 µm layer of copper on one side, covered with a layer photoresist. The bottom side of the laminate is made of a 50 µm thick layer of polyester. Due to its thinness the laminate is quite flexible even before etching. Approximately one square meter of this material was purchased for the project.

Indium-based solder was purchased for solderability tests on the PCB laminate, on the basis that the 118°C melting point of the solder (Indalloy 1E from Indium corporation) is lower than that of polyester. The usefulness of the solder was found to be limited due to the fact that it did not adhere to bare copper or aluminium. Its adhesion to tin-plated components was however good, indicating that it might be usable with tin-plated PCBs.

A standard lead-containing solder with melting point around 188°C was found to work very well if soldering time was kept short. This solder was thereafter favoured over the expensive and cumbersome indium solder.

6.2   Demonstrator selection

A small number of possible supercapacitor demonstrator concepts from relevant fields of industry were presented to the steering committee. The committee recommended a capacitor-powered rechargeable RFID tag to be one of the project demonstrators. The tag was developed in collaboration with Confidex Ltd., who supplied the antenna inlays with the RFID chip already installed. A supercapacitor pack for modular use in electric motor systems was chosen to be the second demonstrator. This application is relevant to Kone Oyj and Kabus Oy.

Additionally, wireless power transfer using both conventional induction and resonant magnetic coupling were demonstrated to the steering committee. A basic wireless power transmitter capable of transferring up to 1 W over a distance of 5 cm was built for this purpose. This transmitter was later used also to evaluate wireless charging of a supercapacitor-assisted RFID tag prototypes.
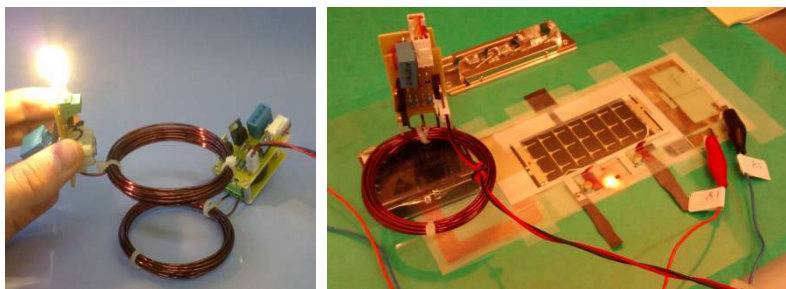
Figure 6.1. Left: Demonstration of wireless power transfer using resonant magnetic coupling. Right: Charging the RFID tag demonstrator in 20 seconds across a distance of 2 cm.

6.3   Demonstrator 1: Rechargeable capacitor-powered semi-passive RFID tag

A functional RFID tag demonstrator was designed and assembled in the project. The tag comprises an RFID inlay received from Confidex Ltd., a supercapacitor manufactured by VTT, a commercial solar panel by PowerFilm Inc. and a charging electronics inlay designed by Aalto University.

To keep tag area small, the supercapacitor, solar panel and tag inlays were stacked on top of each other. The electrical contacts were formed by heat sealing carbon ink contacts against each other. The resistance of such a contact is not negligible, limiting wireless charging speed. For solar panel powered use the resistance is less detrimental, although it may reduce interrogation range somewhat. To counter this either the contacts may be plated with gold instead of carbon or additional buffer capacitance may be added on the inlay.
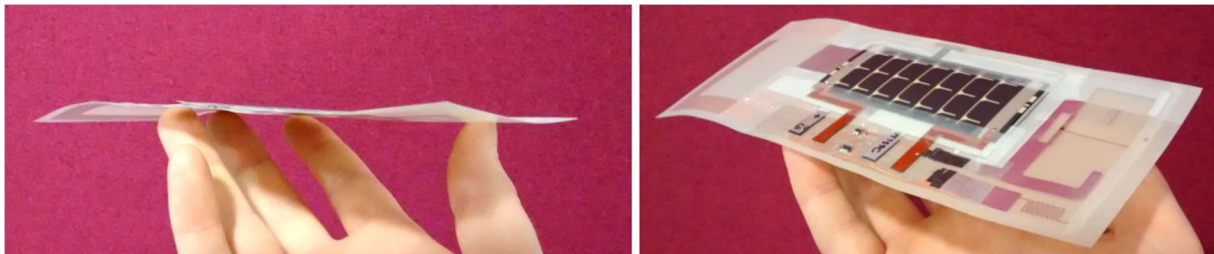

Figure 6.2. The RFID tag demonstrator. Although comprising three separate parts on top of each other the tag is still thin.

The charging electronics inlay contains an inductive wireless charging coil, overvoltage limiting and indication circuitry as well as contact surfaces for forming electrical connections between tag parts. In a final product the RFID antenna and chip could also reside on this inlay.

The circuit diagram of the demonstrator is shown in Figure 6.3. The charging electronics consist of a rectification bridge for the loop antenna, a solar cell reverse current blocking diode, a full charge indicator LED and an overvoltage limiting integrated circuit. Small surface-mounted components with low leakage current were used, resulting in a total current consumption of less than 1 µA below tag voltage of 3.0 V.
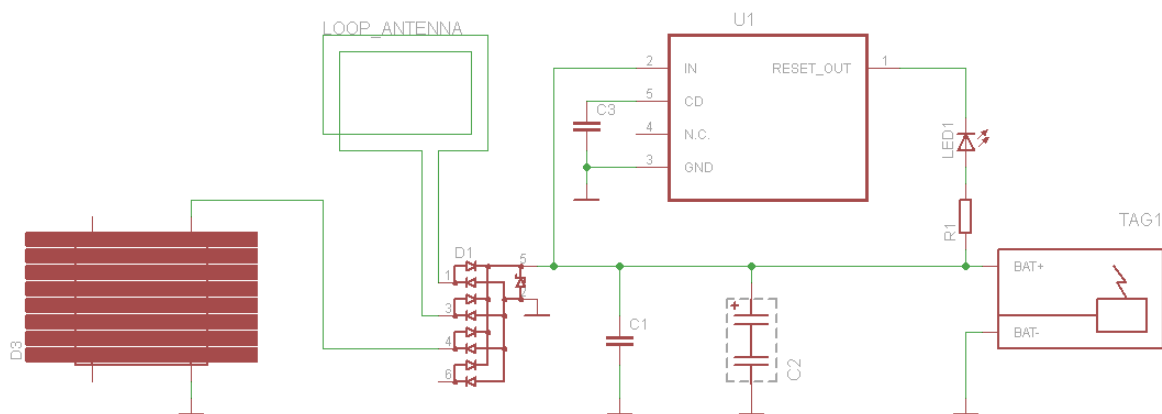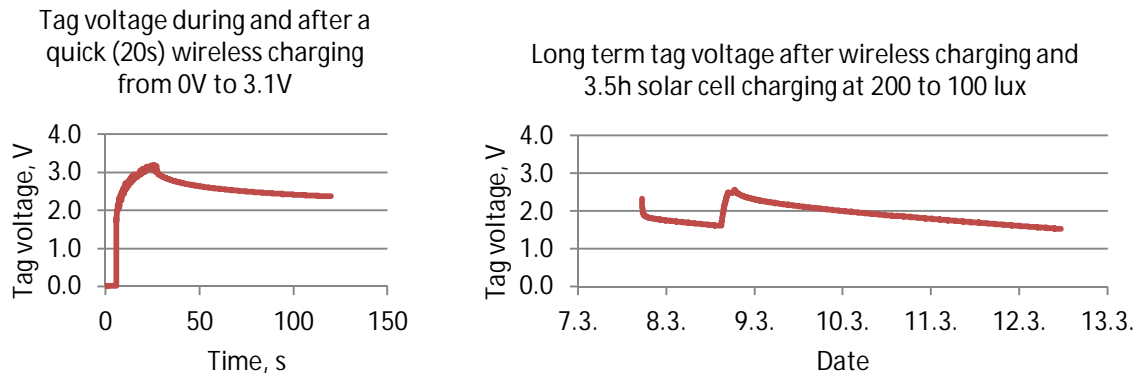

Figure 6.3. Circuit diagram of the assembled RFID tag concept demonstrator

Both solar and inductive wireless charging was successfully tested with the tag demonstrator. A tag with a 0.15 F capacitor was fully charged to 3.1 V across a distance of 2 cm in 20 seconds using induction. However, the slow ionic diffusion rate of the

supercapacitor caused the voltage to quickly drop to a stable level near 2 V after charging was stopped. When charging was performed much more slowly via the solar panel, this drop was much smaller. The voltage of both cases has been plotted in Figure 6.4.

Tag voltage during and after a quick (20s) wireless charging from 0V to 3.1V

Long term tag voltage after wireless charging and 3.5h solar cell charging at 200 to 100 lux

Figure 6.4. Voltage of the tag with a 0.15 F capacitor during and after inductive and solar charging

The operating voltage range of the used RFID chip was from 1.1 V to 3.6 V. While a single capacitor of up to 2.5 V could be used to supply power to the tag, two connected in series were used instead. While this halved the capacitance, a very low leakage current could be achieved instead. Figure 6.4 shows that with the tested dual capacitor the tag could maintain its operating voltage above the 1.1 V level easily for over 72 hours.

During the project, flexible solar cell samples printed on a plastic film were received from VTT. These panels were found to have a good performance in good lighting conditions, but their current output dropped very sharply at lower light comparable to a warehouse (ca. 150 lux). For this reason a commercial thin film solar panel SP4.2-37 by Powerfilm Ltd. was used in the final tag demonstrator.

The tag was demonstrated to the steering committee. The RFID interrogation range was found to be practically same as for a passive tag with a large antenna. This was attributed to bad radio frequency matching between the original RFID antenna and the charging electronics inlay. Charging via solar panel and operation of the overvoltage protection circuit were however successfully demonstrated.

## 6.4   Demonstrator 2: Capacitor pack for motor control applications

The target use case for the second demonstrator was an elevator backup power module. During a building power failure the power module would use its stored energy to move the elevator to a position where the passengers can exit safely. The power required for this operation was reported by Kone Oyj to be around 2-4kW for a duration of a few seconds.

A commercial lithium based automotive battery was used as a starting point for the design. The overall design can be seen in Figure 6.5. A number of capacitor sheets are connected electrically in parallel by a clamp that is tightened by screws. The clamps reside on a 3D-printed support structure, and double as current output terminals. The structure and the capacitors fixed to it are slid inside a simple enclosure. For the demonstrator the enclosure was built from thin polystyrene sheets.
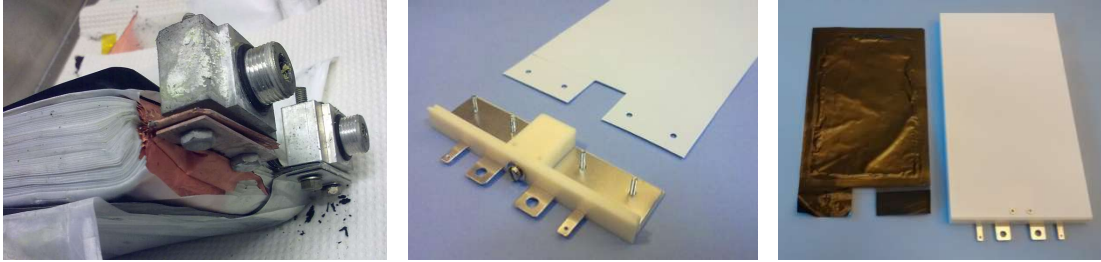
Figure 6.5. Left: Mass parallel termination of planar cells in a lithium ferric phosphate battery for vehicular use (ThunderSky 3.3V battery). Middle: Mass termination adapted for supercapacitor sheets. Right: A complete supercapacitor pack containing up to 20 capacitor sheets stacked in parallel, with one such sheet shown. Capacitance of the pack would range from 200F to 400F, depending on the composition of the capacitors.

A simple mass-lifting demonstrator was built to allow demonstration of the supercapacitor pack, Figure 6.6. The demonstrator would repeatedly raise and lower a mass of 0.5 kg across a distance of 1 m using solely the electric energy stored in the capacitor pack. For the demonstration a 2.5 V capacitor pack consisting of four capacitor sheets of ca. 10 F each in parallel was assembled. While the energy efficiency of the demonstration device was poor (around 10%) it was still able to lift the mass twice up and down before stopping as the pack voltage dropped below 1.2 V.
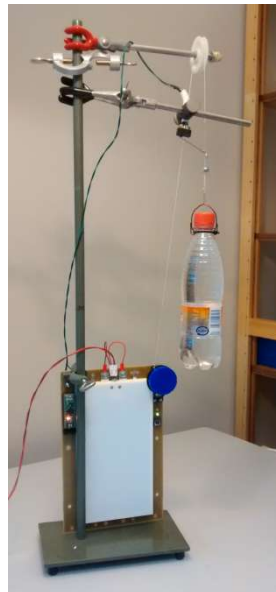
Figure 6.6. Mass-lifting demonstrator for the capacitor pack

6.5   Benchmarking with LiC supercapacitor

JM Energy/JSR Micro Lithium ion capacitors (LiC) are an emerging technology that is beginning to find commercial applications. A limited number of manufacturers supply asymmetric supercapacitors using this concept. Components made by JM Energy were chosen to be tested. Figure 6.7 includes a photograph of these components as well as a schematic of the operating principle. The specified voltage range is 2.2 -3.8 V.

Figure 6.7. LiC supercapacitors and their operating principle.

The 1100 F LiC was tested with 2 A and 50 A currents. The results are shown in table 6.1. The properties were found to be well in line with the specifications given by the manufacturer.

Table 6.1. Electrical properties of LiC supercapacitors

2 A	2 A current				50 A current			
	RT	+50 $^{\circ}$C	-20 $^{\circ}$C	-28 $^{\circ}$C	RT	+50 $^{\circ}$C	-20 $^{\circ}$C	-28 $^{\circ}$C
Capacitance (F)	1113	1064	1021	982	1030	1051	967	890
Efficiency(%)	99.4	99.5	97.0	93.6	95.7	97.4	88.4	85.9
ESR (mΩ)	1*	3*	12*	20*	1.1	0.78	7	11
* Inaccurate because of small IR drop with low current								

The self-discharge rate of the LiC supercapacitors was defined starting from 3.8 V at three different temperatures, Figure 6.8, and also at RT from 3.7 V. Obviously the self-discharge rate was lower when started from 3.7 V.
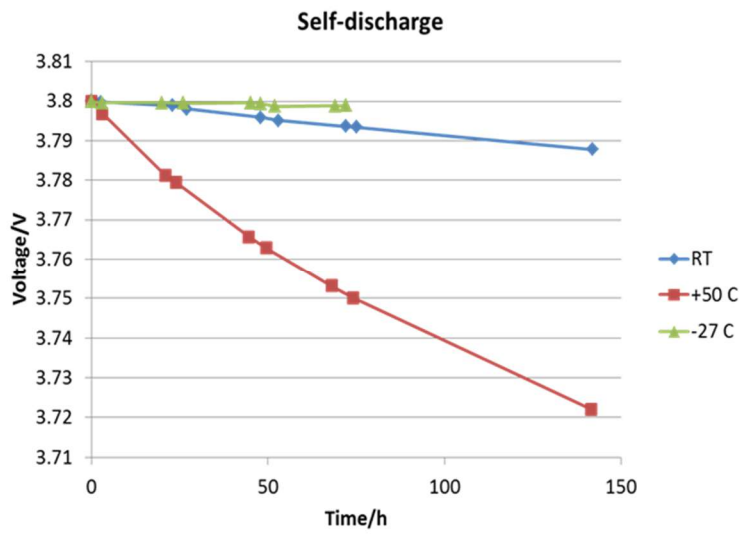
Figure 6.8. Self-discharge rate at various temperatures

7. Conclusions

The commercial activated carbon Norit Super 30 used in most experiments was a good tool in estimating the effect of various process parameters to printing process as well as in electrical, mechanical and life time issues.

The development of MnO_2 and activated carbon materials resulted to new material possibilities in electrodes. The specific capacitance of the processed MnO_2 was clearly higher than that of Norit Super 30. However, the wider potential range of supercapacitors with MnO_2 cathode compared with symmetric activated carbon electrodes was not found to be applicable with constant voltage above 1.3 – 1.5 V.

There was clear progress in the aqueous electrolytes especially in finding alternatives for NaCl salt and in developing gel-like systems. The advantages are especially in the life time of the supercapacitor and in making the assembling simpler.

Several ionic liquids (IL) based on organic electrolytes were used, and especially new environmentally friendly ionic liquids were shown to work well in combination with the Chitosan/activated carbon electrodes. Clear life time related improvements in the case of using Ecoeng 212 electrolytes were achieved.

Supercapacitors using e-beam curing to make the solid electrolyte were realized. Due to interaction of the monomers with the activated carbon electrodes these have lower performance (1/10 of normal capacitance values) but might be usable in applications where this is not crucial.

A new and simpler device layout, the lateral supercapacitors were made. They were manufactured by screen printing and had roughly 1/5 of the capacitance and 1/10 of the maximum power of a face-to-face assembled supercapacitor of the same area.

Pilot scale roll-to-roll experiments gave large amount of practical data of the printability of the inks and of the required process parameters such as printing speed and furnace temperatures. The pilot experiments showed that the production by printing is feasible. The printing properties of inks including long drying time requirements are not yet completely ready for the needs of flexible fabrication of supercapacitors in production scale.

The capacitance range of the supercapacitors made during the project was 0.1 – 20 F. The capacitance can be down- or up-scaled when needed. The ESR level obtained was down to 1 Ω/cm^2. The efficiency was dependent on the structure and materials chosen. Values up to 97 % were reached. The voltage over a single supercapacitor cell is dependent on electrolyte: with aqueous electrolyte 1.2 V is achieved and with organic electrolyte 2.7 V. With ionic liquid over 3 V can be reached. The cycle life of supercapacitors with aqueous and organic electrolytes was tested: the cycle life clearly exceeds 50000 cycles.

Life cycle analysis (LCA) was conducted on the basis of data obtained from pilot scale experiments and literature data. The analysis covered the manufacturing, use and disposability of printed supercapacitors.

A number of demonstration application concepts were presented. Of these, two were chosen to be developed as final project demonstrators: a capacitor pack for motorized applications and a wirelessly rechargeable supercapacitor-assisted RFID tag. A functional tag demonstrator was built, that could be recharged wirelessly either fast (in ca. 20 seconds) via induction or slower (hours, depending on the lighting intensity) via a solar panel. Also, a

functional high capacity capacitor pack containing up to 20 large size capacitors sheets was assembled and demonstrated.

As a benchmark a commercially available 1100 F lithium ion capacitor was characterized. The properties were found to be in accordance with data sheets.